Lehigh University
Lehigh Preserve

Theses and Dissertations

1989

Mixing enhancement in flow past rectangular cavities as a result of a periodically pulsed forcing function /

Jeffrey S. Perkins
Lehigh University

Follow this and additional works at: https://preserve.lehigh.edu/etd

 Part of the Mechanical Engineering Commons

Recommended Citation
Perkins, Jeffrey S., "Mixing enhancement in flow past rectangular cavities as a result of a periodically pulsed forcing function /" (1989). *Theses and Dissertations*. 4970.
https://preserve.lehigh.edu/etd/4970

This Thesis is brought to you for free and open access by Lehigh Preserve. It has been accepted for inclusion in Theses and Dissertations by an authorized administrator of Lehigh Preserve. For more information, please contact preserve@lehigh.edu.

MIXING ENHANCEMENT IN FLOW PAST RECTANGULAR CAVITIES AS A RESULT OF A PERIODICALLY PULSED FORCING FUNCTION

by

Jeffrey S. Perkins

A Thesis

Presented to the Graduate Committee

of Lehigh University

in Candidacy for the Degree of

Master of Science

in

Mechanical Engineering

MIXING ENHANCEMENT IN FLOW PAST RECTANGULAR CAVITIES AS A RESULT OF A PERIODICALLY PULSED FORCING FUNCTION

Jeffrey S. Perkins

Abstract-

Periodic elimination of the shear layer separating the mainstream and recirculatory regions in flow through a multi-cavity channel is possible by imposing a pulsatile forcing function on the otherwise steady fluid motion. Numerical and experimental results are correlated to show that pulsing the flow during half of a cycle leads to the destruction of the trapped vortex while simultaneously generating its replacement. During the other half of the cycle, where there is only steady flow, the new vortex grows to fill the cavity and protrudes into the mainstream, thus further enhancing mainstream and cavity mixing. The fluid motion is characterized by three non-dimensional parameters: a Reynolds number based on the steady velocity component, a Strouhal number based on the unsteady velocity component and a frequency parameter based on the frequency of oscillation. The effect of each parameter on fluid exchange between the mainstream and the cavity is discussed.

CERTIFICATE OF APPROVAL

This thesis is accepted and approved in partial fulfillment of the requirements for the degree of Master of Science.

Dec 13th, 1988

(date)

Kyra D. Stephens

Professor in Charge

F. Erdogan

Chairman of Department

ACKNOWLEDGEMENTS

This paper is dedicated to my parents John S. and Sandra R. Perkins. Their support has helped push me through the more difficult periods of the work required to form this thesis.

Special thanks are extended to Dr. Kyra D. Stephanoff for providing direction throughout this project. Dr. Bruce T. Murray formulated the source code necessary to do the finite difference solutions as well as teaching me much of what I know about finite difference approximations. The experimental procedure was developed by Dr. Vivek Mansingh and I received invaluable photographic advice and use of equipment from my father, John S. Perkins.

This work has been supported through grants from AT&T, the Semiconductor Research Corporation, and the National Science Foundation (#MSM-8352244).

TABLE OF CONTENTS

LIST OF FIGURES

NOMENCLATURE

d	Cavity depth
F_p	Frequency parameter
h	Channel width
l	Cavity length
L	Geometric periodicity length
Re_p	Pulsatile Reynolds number
Re_s	Steady Reynolds number
S_t	Strouhal number

LIST OF FIGURES

NOMENCLATURE

d	Cavity depth
F_p	Frequency parameter
h	Channel width
l	Cavity length
L	Geometric periodicity length
Re_p	Pulsatile Reynolds number
Re_s	Steady Reynolds number
S_t	Strouhal number

Abstract-

Periodic elimination of the shear layer separating the mainstream and recirculatory regions in flow through a multi-cavity channel is possible by imposing a pulsatile forcing function on the otherwise steady fluid motion. Numerical and experimental results are correlated to show that pulsing the flow during half of a cycle leads to the destruction of the trapped vortex while simultaneously generating its replacement. During the other half of the cycle, where there is only steady flow, the new vortex grows to fill the cavity and protrudes into the mainstream, thus further enhancing mainstream and cavity mixing. The fluid motion is characterized by three non-dimensional parameters: a Reynolds number based on the steady velocity component, a Strouhal number based on the unsteady velocity component and a frequency parameter based on the frequency of oscillation. The effect of each parameter on fluid exchange between the mainstream and the cavity is discussed.

Introduction-

Internal fluid motion past rectangular cavities such as that shown in Fig. 1, exists in devices such as electronic components on circuit boards and ribbed heat exchangers in cross flow. In these devices, steady forcing of the flow causes separation regions to form in the cavities. As a result of the steady fluid motion past the mouth of each cavity, there is a strong division between the straight and parallel streamlines found in the driving flow and the recirculating streamlines within the cavity. Transverse flow across the shear layer between the cavity and channel is absent. This lack of mixing inhibits effective heat removal from the cavity fluid, which in turn diminishes the removal of heat from the generating surfaces.

To promote mixing of the fluid between the two regions, the shear layer must be severed by some means, showing interaction of the mainstream with the fluid trapped in the cavity. Several studies [1,2,3] show that forcing the flow sinusoidally leads to excellent mixing of the mainstream with that of a separated region. However, the sinusoidal motion has no net flow rate, which is needed to remove heat from the system. Superposing unidirectional fluid motion onto the oscillatory motion will cause heat removal since the unsteady component enhances lateral mixing, while the steady component provides transport of heat away from the cavity and out of the system. The effect on the flow field of one type of unsteady forcing is the focus of the present study. Although the results presented are restricted to the flow analysis, the ultimate goal of the study is to determine the optimum conditions for efficient heat removal.

Forcing of the fluid can be accomplished by superposing an oscillatory component on a steady flow, however, a sinusoidal variation will at some times add to the forcing flow rate while at other times it will lessen it. The reduction in the flowrate

will decrease the amount of heat removal in a system, thus if increased mixing can result by using the additive portion of the oscillatory component alone, there is no reason to use the detractive portion. The resulting forcing function varies sinusoidally as an additive pulse superposed onto the steady flow for half of a cycle, while for the other half cycle, only a steady flow exists (see Fig. 2).

The fluid motion past the periodically repeated rectangular cavities, used in the experimental and numerical parts of the study, is assumed to be fully developed. This condition is easily imposed numerically by defining periodic boundary conditions. In the experiments, fully developed flow occurs after the sixth of seventh cavity such that the flow past one cavity is the same as that past any other cavity.

Two-dimensional laminar fluid motion is assumed in the experiments and the numerical analysis which is justified if the geometry is infinite in breadth. Numerically, this assumption reduces the number of governing equations of motion by one. Experimentally, the two-dimensional flow assumption is approximated by an experimental channel with a large breadth dimension relative to the channel width such that the boundary layers in the breadth dimension do not affect the flow. The breadth to width aspect ratio is 15:1 in the experimental channel.

Literature Review-

The present study examines periodically pulsed planar fluid motion past a series of rectangular cavities. Similar studies on planar flow past geometries with periodic cavities and periodic forcing functions have been reported numerically in Sobey (1980, 1982) and experimentally in Stephanoff, Sobey, and Bellhouse (1980). Geometries used in these investigations include channels with sinusoidally varying walls, both symmetric and asymmetric; channels with semi-circular scallops on the walls; and channels with rectangular cavities. In each paper the fluid motion resulting from a sinusoidal forcing with no mean velocity is discussed. It is found that during a cycle, recirculatory fluid motion (a vortex) develops within the cavities. The vortex in each cavity grows with deceleration and is then ejected into the center of the channel during flow reversal. Fluid previously comprising this vortex is then entrained in the accelerating mainstream and is transported away from the cavity, provided the magnitude of the oscillation is sufficient.

Subsequent numerical work by Ralph (1986) on oscillatory motion through channels with sinusoidally varying walls reiterates the results discussed above but shows that neglecting effects of a flow's time-history is not a uniformly valid assumption, as implied in Sobey (1980). It is shown that when the vorticity transport is low, the ejected vortex is not necessarily destroyed by the accelerating mainstream. Effects of the ejected vortex can persist well after the onset of reversal.

Similar numerical work by Savvides and Gerrard (1984), illustrates oscillatory motion in a channel with walls varying as triangle waves. Steady forcing of the fluid past the periodic geometry shows that for a Reynolds number above a critical value, the mainstream appears largely unaffected by the presence of the irregular wall, aside from the local relaxation of the no-slip condition. Streamlines in the mainstream are

parallel and a shear layer spans each triangular cavity. The fluid motion within a cavity forms a well-defined vortex driven by the shear layer interface. This seems to be the only interaction between the two regions for a steady forcing function. Of primary interest are the solutions for oscillatory motion where an oscillatory component is imposed upon a steady flow. It is shown that when the steady and oscillatory components are of the same order of magnitude, periodic ejection of recirculatory fluid from a cavity occurs and is followed by a subsequent reformation of the vortex in this separated region.

The results presented in the studies discussed above have importance in applications needing enhanced transport of some quantity such as mass or heat from a separated region. Not only can the trapped fluid be ejected into the mainstream through the positive effects of oscillatory motion on separated regions, but by superimposing an oscillatory motion on a steady flow, the mass or heat energy can be washed downstream and eventually out of the system. Possible applications include: 1) enhancing heat transfer from electronic components mounted on a circuit board; 2) enhancing heat transfer from ribbed heat exchangers experiencing a cross flow; and 3) removal of a substance which settles in notches on a wall of a device.

Numerical solutions by Ghaddar, et. al. (1986), further illustrates fluid motion through a flat wall channel with rectangular cavities on one of the flat walls. As in previous studies, the steady flow solutions show a well defined vortex within the cavity and a cavity-spanning shear layer is present. In general, the center of the vortex is shifted downstream of the center of the cavity and again the mainstream and recirculatory regions are largely isolated from each other. Other than driving the cavity motion through this interface, the cavity and mainstream are essentially independent flows.

As in the work by Savvides and Gerrard, Ghaddar, et. al. examine motion with a steady and an oscillatory component. However, in the Ghaddar et. al. study the magnitude of the oscillatory component is much less than that of the steady component. The sinusoidal variation is introduced as a small perturbation to the steady flow rate for moderate Reynolds numbers. It is shown that self-sustained oscillations develop in the shear layer which trigger the onset of transition to turbulence at Reynolds numbers lower than that which occurs for steady forcing of the fluid. As a result of the shear layer oscillations, there is a significant change in the flow structure in the vicinity of the cavity-mainstream interface. The self-sustaining oscillations indicate stronger interactions between the two regions than that of pure steady flow and are found to enhance the transport of heat from the cavity [16].

In this study, periodic fluid motion past a geometry similar to that used in Ghaddar, et. al., i.e. spatially fully developed flow past rectangular cavities, is examined, although the nature of the flow field is quite different. The primary objective is enhancement of transport characteristics of flow past cavities, which leads to a slightly different flow profile. The fluid motion contains a steady component with a superimposed unsteady component of the same order of magnitude where the unsteady component is an additive sinusoidal pulse which exists for half of a cycle. Numerical and experimental comparisons will be made from results contained herein to results from the studies discussed above.

Flow Characterization in Dimensionless Parameters-

By grouping certain variables together, which describe the fluid motion and geometry, parameters can be formed such that all dimensional dependence cancels out. Choosing these dimensionless parameters properly yields an excellent means of comparing different flows without having to analyze each in detail. Since the parameters are dimensionless they apply to different dimensional scales without variation of the fluid motion; in other words, if two devices have the same dimensionless parameters, the flow structure will be the same.

In this study the characterization of the flow field will be the mean velocity U(t) imposed by the forcing function. As previously described, the forcing function is a sinusoidal variation on a steady flow where only additive effects are used, resulting in steady forcing for half of a cycle with period T, and a steady plus a sinusoidal pulse for the other half cycle. Figure 2 shows a typical waveform which would exist in a parallel walled channel, which can be described as

$$U(t) = \begin{cases} U_s & 0 \le \frac{t}{T} \le 0.5 \\ U_s + U_p \sin[\, 2\pi\, (\frac{t}{T} - 0.5)\,] & 0.5 \le \frac{t}{T} \le 1.0 \end{cases}$$

where U_s is the velocity due to the steady component, and U_p is amplitude of the sinusoidal pulse present for the second half cycle. The forcing function accelerates the fluid from a velocity of U_s to a value of $U_s + U_p$ during $0.5 \le \frac{t}{T} \le 0.75$, and decelerates it to U_s for $0.75 \le \frac{t}{T} \le 1.0$.

For convenience, a new time variable, τ, is formed such that $\tau = \frac{t}{T}$. Since the flow is periodic and fully developed in the sense that the flow at $\tau = \tau_1$ is exactly the same as that at $\tau = \tau_1 + T$, the variable τ is normalized such that $0 \le \tau \le 1.0$.

In this study, the geometry and the type of forcing function are held constant. There are three independent variables U_s, U_p, and T, which suggests that three independent dimensionless parameters form the necessary basis to describe a uniquely determined flow. Since the velocity is assumed to be the superposition of a steady velocity and a time dependent velocity, the describing parameters are chosen such that time dependent effects are separate from effects due to the steady flow. The steady flow is characterized by a steady Reynolds number such that

$$Re_s = \frac{hU_s}{\nu}$$

where h is the channel width and ν is the kinematic viscosity, which is kept fixed.

It is unclear whether U_s, U_p, or $U_s + U_p$ should be used when defining the Strouhal number, S_t. Since the parameter normally describes time dependent motion, it is chosen to be defined as

$$S_t = \frac{f\,h}{U_p}.$$

In support of this choice it can be shown by integrating U(t) from $0 \le \tau \le 1.0$ that S_t is function of only one variable, the volume of fluid added to the flow per cycle, Q_p, during the pulse. Each of the three defining parameters will similarly be a function of only one variable.

In addition to Re_s and S_t, a third parameter is necessary to form a basis for full characterization of the flow. As this third dimensionless quantity, a frequency parameter, F_p, is used which is only a function of the frequency of oscillation. F_p is defined as

$$F_p = \frac{f\,h^2}{\nu}.$$

The flow is fully characterized by Re_s, S_t, and F_p, but there is a fourth parameter which becomes useful in comparisons. This parameter is a pulsatile Reynolds number of the form

$$Re_p = \frac{hU_p}{\nu}.$$

Using the previous definitions for F_p and S_t, Re_p can be expressed as

$$Re_p = \frac{F_p}{S_t}.$$

In analyzing the following results, it is important to realize that the pulsatile Reynolds number is achieved at only one instant in the cycle, at the peak of the input pulse, when $\tau = 0.75$. Nevertheless, mixing is a very strong function of the ratio of this pulsatile Reynolds number to the steady Reynolds number.

Using the three initial parameters, Re_s, F_p, and S_t, yields a useful set of directly applicable relations. In the flow visualization experiments U_s, f, and the volume of fluid added per pulse, Q_p, are adjustable such that Re_s, F_p, and S_t are directly measured. The sinusoidal pulse is enforced with a piston such that Q_p is controlled by adjusting the piston's stroke. The choices for the parameterization are therefore shown to be good in that each parameter is a function of only one variable, and convenient in that the independent variables are, in general, easily measurable quantities.

Experimental Setup-

The flow visualization experiments use water as the working fluid in a closed channel constructed of plexiglas. As shown in Fig. 3, the channel consists of five sections: a diffuser, a long upstream flat wall section to insure fully-developed plane Poiseuille flow prior to the test section, a replaceable test section, a long downstream flat wall section, and a convergent section. The test section and flat wall sections have inner dimensions of 22.9 x 1.52 cm, the former being the vertical, yielding an aspect ratio of 15:1.

The fluid enters the piping system through one of two inlet pipes shown in Fig. 4. Inlet #1 supplies fluid used to generate a pulse in the velocity profile while inlet #2 supplies a constant head steady flow. Valves A and B shown in Fig. 4 are one-way valves which prohibit fluid motion up either of the two inlet pipes. The piston, which is connected to a Scotch yoke mechanism, oscillates at a frequency determined by the speed setting on the driving motor's controller. As the piston retracts, fluid is drawn through valve A from inlet #1; valve C, also a one-way valve, prevents the piston from drawing fluid from inlet #2 or the channel. The fluid drawn into the piston chamber is expelled through valve C when the piston moves toward the channel. This fluid joins the steady component which is supplied throughout the cycle. Immediately downstream, the velocity profile appears steady for the first half cycle when the piston draws fluid from inlet #1 and then pulsatile during the second half cycle. The resulting mean velocity profile is shown in Fig. 2. While the flow rate of the steady component is controlled by a needle valve (not shown) on inlet #2, the flow rate of the pulsatile component depends on the frequency of oscillation of the piston and its stroke (the volume of fluid expelled during each stroke).

After the steady and pulsatile flows merge, the fluid passes through the diffuser and then enters the channel. A three inch length of honeycomb and the following long flat wall section straighten the flow prior to entering the test section. Upon entering the test section, the walls are still flat until the first of 15 bars mounted transversely on one of the vertical walls. Extending from the top of the channel to the bottom, the bars have a square cross-section of 0.64 cm on a side and are spaced by a gap of 1.27 cm (see Figs. 1 and 5a). Each cavity formed between the bars is 0.64 cm deep and 1.27 cm long. Since the bars protrude into the channel the effective channel width, h, is 0.89 cm. From Fig. 5a, the geometric periodicity length, L, is 1.91 cm. As the fluid passes the first few bars it adjusts to the spatially varying boundary along one wall and becomes fully developed by the seventh cavity. All photographs in the study are from the ninth cavity where the flow is fully developed.

As the fluid exits the test section it enters another long parallel-wall section and then a nozzle with the same dimensions as the diffuser. The flow converges to the exit pipe which leads to a reservoir. The fluid in the reservoir is then pumped up to the two feed tanks which supply inlets #1 and #2.

Flow rates are measured with a one U.S. gallon jug and a stopwatch. During an experiment, the steady flow rate is measured before the Scotch yoke is started. After the yoke is started, the fluid motion needs a few minutes to reach equilibrium conditions and then the total flow rate is measured. From the period of oscillation, the stroke of the piston, and the two flow rate readings, the dimensionless numbers, Re_s, S_t, and F_p are calculated.

Natural pearl essence, comprised of flake-like luminescent particles which have a settling time of roughly two hours in water, is mixed into the water so that the fluid motion is visible. The quantity of pearl essence added is dependent upon the

mixing between the mainstream and fluid in the cavity. If mixing in the cavity is good, a large number of particles enter the cavity so the fluid motion in both the cavity and mainstream is visible. However, if mixing between the two regions is poor, only a small number of particles enter the cavity, which does not illuminate this region sufficiently. As a result, more pearl essence must be added to the fluid for poorly mixing flows to illuminate the cavity region sufficiently.

While taking pictures, the entire test section is masked with an opaque material except for 1) a thin slit 0.64 cm wide which passes a horizontal plane of light at the centerplane of the channel, and 2) the top of the section where the camera sits. Light from a 750 Watt halogen spot light passes through a cylindrical plano-convex lens before entering the thin slit in the masking material. The plano-convex lens converges the light into an intense parallel beam so that the particles at the centerplane are highly illuminated.

A Canon A1 35mm SLR camera with a 105mm macro lens is used for the photography. The camera is attached to an adjustable height bracket which is fixed to a platform on rails directly above the channel. During filming the camera points down through the top of the test section and is focused on the illuminated centerplane. Black and white Kodak Technical Pan film, which is a high resolution, variable speed film, is used at a speed of 160 ASA and is developed using a high contrast process.

An external triggering device, connected to the camera's high speed motor drive, controls the timing of the photography. A magnetic switch is mounted on the flywheel of the Scotch yoke to provide a position reference signal for the triggering sequence. From this reference signal, the triggering device calculates the period of oscillation and emits a trigger signal to the motor drive at a specified time in the cycle.

The error involved in correct placement of the magnetic switch is 2-3 % of the period of oscillation.

Correct shutter speed is crucial to obtaining the best visualization of the time dependent flow. Instantaneous streamlines, which are in reality particle pathlines, will only become visible if the particles travel a sufficient distance during the opening of the shutter. While long shutter speeds let excellent pathlines of individual particles be photographed, accurate results require that the shutter speed can only be a small fraction of the cycle time. Shutter speeds must be no more than five percent of the total cycle time, which ranges from two to six seconds. Depending on the period of the cycle, shutter speeds of $^1/_4$, $^1/_8$, and $^1/_{15}$ of a second are used.

For cases involving strong mixing in the cavity throughout the cycle, velocities encountered within the cavity are of the same order as those in the mainstream, thus a particle in either field travels the same distance in a specified time. However, for steady flow and those which are similar to steady flow, velocities in the cavity are much lower than those in the mainstream. Shutter speeds for these cases must be at least $^1/_4$ second to show any noticeable particle motion within the cavity and even when the shutter speed is this long it is often difficult to capture the flow structure in the cavity region.

Numerical Analysis-

The numerical solutions, as well as the experimental results, model a two-dimensional, incompressible flow past a uniform series of rectangular cavities. Defining quantities in the x,y plane of a Cartesian coordinate system, the flow field is determined by calculating the velocity components u in the streamwise (x) direction, and v in the transverse (y) direction. Fluid properties such as the kinematic viscosity, ν, are assumed to be constant over the range of flow conditions studied and under the incompressible assumption, the density, ρ, is also a constant. Body forces, such as those due to gravity are assumed to act in a direction normal to the plane of motion and thus, not affect the flow. Fluid motion is then governed by the two-dimensional Navier-Stokes equations, which require the conservation of linear momentum in each of the coordinate directions:

$$\frac{\partial u}{\partial t} + u\frac{\partial u}{\partial x} + v\frac{\partial u}{\partial y} = -\frac{1}{\rho}\frac{dP}{dx} + \nu\left(\frac{\partial^2 u}{\partial x^2} + \frac{\partial^2 u}{\partial y^2}\right) \tag{1}$$

$$\frac{\partial v}{\partial t} + u\frac{\partial v}{\partial x} + v\frac{\partial v}{\partial y} = -\frac{1}{\rho}\frac{dP}{dy} + \nu\left(\frac{\partial^2 v}{\partial x^2} + \frac{\partial^2 v}{\partial y^2}\right) \tag{2}$$

where P is the pressure. In addition to (1) and (2), a continuity of mass equation for two-dimensional flow is

$$\frac{\partial u}{\partial x} + \frac{\partial v}{\partial y} = 0\,. \tag{3}$$

The equations of fluid motion are solved by ridding their dependence on dimensional quantities such as length, time, and mass. The dimensionless parameters, which act as coefficients, determine the solution of the fluid motion. Flows with identical parameters yield identical solutions, independent of different dimensional scales. Nondimensionalization scales each term in the equations (1), (2), and (3) by a characteristic quantity of the same dimensions. For example, the term $\frac{\partial u}{\partial x}$ in eqn. (3)

would be nondimensionalized by dividing u by some characteristic velocity, U, and x by some characteristic length, H. As this is done to each term in (1), (2), and (3), common terms are canceled out leaving each term dimensionless. Certain terms will retain coefficients formed by groups of these characteristic quantities. It is these groups of quantities, or dimensionless parameters, which uniquely determine the flow field solution for a given set of boundary conditions.

In the domain shown in Fig. 5a, all length dimensions are scaled on the dimensional channel width, h. Defining the *dimesionless* channel width, *h* as 1.0, the scaled cavity depth, *d* is 0.7, the cavity length, *l*, is 1.4, and the geometric periodicity length, *L*, is 2.1. In a similar way, the length variables x and y are nondimensionalized by forming the quantities

$$x = \frac{x}{h} \qquad y = \frac{y}{h} . \tag{1}$$

Since choosing the scale factor is somewhat arbitrary, the equations are not effectively changed in any way. U_p is chosen as the velocity scale factor and u and v are nondimensionalized as follows,

$$u = \frac{u}{U_p} \qquad v = \frac{v}{U_p} . \tag{2}$$

Although not apparent here, U_p is used as the scaling velocity because it yields a convenient form of the boundary conditions which are enforced on the numerical solution. As before, time is nondimensionalized on the period of oscillation T as

$$\tau = \frac{t}{T} . \tag{3}$$

The Navier-Stokes equations, written in their nondimensional form, become

$$S_t \frac{\partial u}{\partial \tau} + u \frac{\partial u}{\partial x} + v \frac{\partial u}{\partial y} = - \frac{\partial P}{\partial x} + \frac{1}{Re_p} \left(\frac{\partial^2 u}{\partial x^2} + \frac{\partial^2 u}{\partial y^2} \right) \tag{4}$$

and

$$S_t \frac{\partial v}{\partial \tau} + u \frac{\partial v}{\partial x} + v \frac{\partial v}{\partial y} = - \frac{\partial P}{\partial y} + \frac{1}{Re_p} \left(\frac{\partial^2 v}{\partial x^2} + \frac{\partial^2 v}{\partial y^2} \right). \qquad (5)$$

where the coefficients S_t and Re_p are as defined previously. In eqns. (4) and (5) the terms on the left hand side of the equation represent the total change in the local velocity due to unsteady flow and convected effects. The terms on the right represent the effects of pressure variations and viscous effects in the absence of body forces such as gravity. The continuity equation in dimensionless form is

$$\frac{\partial u}{\partial x} + \frac{\partial v}{\partial y} = 0 . \qquad (6)$$

As is common in calculations of two-dimensional incompressible flows, the equations of motion, written in terms of the primitive variables, u,v, and P, are transformed into equations in terms of the stream function, ψ, and the vorticity, ω. The stream function is defined such that

$$u = \frac{\partial \psi}{\partial y} \qquad v = - \frac{\partial \psi}{\partial x} \qquad (7)$$

which identically satisfies (6), and ω is defined as

$$\omega = \frac{\partial v}{\partial x} - \frac{\partial u}{\partial y} . \qquad (8)$$

By cross-differentiation, the Navier-Stokes equations can be replaced by a single equation for the vorticity,

$$S_t \frac{\partial \omega}{\partial \tau} + u \frac{\partial \omega}{\partial x} + v \frac{\partial \omega}{\partial y} = \frac{1}{Re} \left(\frac{\partial^2 \omega}{\partial x^2} + \frac{\partial^2 \omega}{\partial y^2} \right) \qquad (9)$$

and from the definition of ω and ψ,

$$\frac{\partial^2 \psi}{\partial x^2} + \frac{\partial^2 \psi}{\partial y^2} = - \omega . \qquad (10)$$

The stream function-vorticity formulation reduces the number of equations and avoids the need to deal with the pressure term in the primitive variable equations. This is useful here, since the pressure field is not of direct interest for the present study.

Notice that (9) is similar to (4) and (5) so the equation can be thought of as a balance between the changes in vorticity due to unsteady and convective effects and the vorticity diffusion.

Equations (9) and (10) are solved by approximating the each with a finite difference solution at node points on a grid overlaid on the domain shown in Fig. 5b. At each time step, (9) and (10) are solved using information from the previous two time steps. The solution then proceeds in time throughout each cycle.

Leapfrog / Dufort-Frankel, an explicit, unconditionally stable finite difference method which is second order accurate in both space and time, is used to solve the vorticity equation at each time step. Using the subscripts (i,j) to denote (x,y) spatial position, the superscript (n) to denote the time step, and writing u and v in terms of ψ, the terms on the left hand side of eqn. (9) become

$$\frac{\partial \omega}{\partial \tau} = \frac{\omega_{i,j}^{n+1} - \omega_{i,j}^{n-1}}{2\,\Delta\tau} \tag{11}$$

$$u\frac{\partial \omega}{\partial x} = \left(\frac{\psi_{i,j+1} - \psi_{i,j-1}}{2\,\Delta y}\right)\left(\frac{\omega_{i+1,j}^{n} - \omega_{i-1,j}^{n}}{2\,\Delta x}\right) \tag{12}$$

$$v\frac{\partial \omega}{\partial y} = -\left(\frac{\psi_{i+1,j} - \psi_{i-1,j}}{2\,\Delta x}\right)\left(\frac{\omega_{i,j+1}^{n} - \omega_{i,j-1}^{n}}{2\,\Delta y}\right) \tag{13}$$

and using the Dufort-Frankel method of replacing ω_{ij}^{n} by its average at times n-1 and n+1 in the central differencing of the diffusion terms,

$$\frac{\partial^2 \omega}{\partial x^2} = \left(\frac{\omega_{i+1,j}^{n} - \omega_{i,j}^{n+1} - \omega_{i,j}^{n-1} + \omega_{i-1,j}^{n}}{(\Delta x)^2}\right) \tag{14}$$

$$\frac{\partial^2 \omega}{\partial y^2} = \left(\frac{\omega_{i,j+1}^{n} - \omega_{i,j}^{n+1} - \omega_{i,j}^{n-1} + \omega_{i,j-1}^{n}}{(\Delta y)^2}\right). \tag{15}$$

Defining the constants

$$r = \frac{\Delta x}{\Delta y}, \quad C = \frac{\Delta \tau}{2 \Delta x \Delta y}, \qquad D = \frac{2 \Delta \tau}{Re (\Delta x)^2}, \tag{16}$$

combining eqns. (11)-(15) into eqn. (9) and writing all n+1 time levels on the left hand side, the finite difference form of the vorticity equation is

$$\begin{aligned} \left(S_t + D (1+r^2) \right) \omega_{i,j}^{n+1} = & \left(S_t - D (1+r^2) \right) \omega_{i,j}^{n-1} \\ & + C \left[(\psi_{i+1j} - \psi_{i-1j}) (\omega_{i\,j+1}^{n} - \omega_{i\,j-1}^{n}) - (\psi_{i,j+1} - \psi_{i,j-1}) (\omega_{i+1j}^{n} - \omega_{i-1j}^{n}) \right] \\ & + D \left[\omega_{i+1j}^{n} + \omega_{i-1j}^{n} + r^2 (\omega_{i\,j+1}^{n} + \omega_{i\,j-1}^{n}) \right] \end{aligned} \tag{17}$$

which can be solved explicitly for $\omega_{i,j}^{n+1}$ in terms of ω and ψ values at the two previous time levels, n and n-1.

A standard five-point central difference form of the Poisson equation for the stream function (10), yields

$$\frac{\psi_{i+1,j} - 2 \psi_{i,j} + \psi_{i-1,j}}{(\Delta x)^2} + \frac{\psi_{i,j+1} - 2 \psi_{i,j} + \psi_{i,j-1}}{(\Delta y)^2} = - \omega_{i,j} . \tag{18}$$

Eqn. (18) is solved iteratively by successive-over-relaxation (SOR) in the form

$$\psi_{i,j}^{k+1} = \frac{\Omega}{2(1+r^2)} \left[r^2 \psi_{i,j-1}^{k+1} + \psi_{i-1j}^{k+1} + r^2 \psi_{i\,j+1}^{k} + \psi_{i+1j}^{k} + (\Delta x)^2 \omega_{i,j} \right] + (1-\Omega) \psi_{i\,j}^{k} \tag{19}$$

where the k index is the iteration level and $\Omega = 1.83$ is the SOR acceleration parameter. In eqn. (19) values of ψ at the iteration level k+1 at (i,j-1) and (i-1,j) are used to apply the most recently acquired information, while values at the iteration k are used for nodes (i,j), (i+1,j), and (i,j+1) which have not yet been updated to the k+1 level. At each time step eqn. (19) is iterated until the maximum variation on ψ between iterations is less than 1×10^{-4}.

Necessary conditions that must be met on the boundary of the computational domain are that 1) ω and ψ must be periodic over the periodicity length, L, i.e.

$$\psi (0,y) = \psi (L,y) \qquad \omega (0,y) = \omega (L,y) \tag{20}$$

and 2), u and v must vanish at solid surfaces which requires

$$u = \frac{\partial \psi}{\partial y} = 0 \qquad\qquad v = \frac{\partial \psi}{\partial x} = 0 \tag{21}$$

along the top and bottom walls. From conditions imposed by (21), ψ must be a constant along solid surfaces.

To determine the constant values of ψ along each wall, a relation for the flow rate $q(\tau)$ is found by integrating the u velocity component from the bottom surface to the top, that is

$$q(\tau) = hU(\tau) = \int u(y)\, dy\,, \tag{22}$$

which, by the definition of ψ in (7) can be changed to

$$q(\tau) = hU(\tau) = \int d\psi = \psi_2 - \psi_1\,. \tag{23}$$

For convenience, the value of ψ along the top surface (the more complicated surface due to changes in spatial direction), ψ_2, is set to zero. By (23), ψ_1 along the bottom surface is then equal to the negative of the flow rate at any time, τ. The dimensionless form of the boundary condition yields,

$$\psi(x,0) = -\begin{cases} \dfrac{Re_s}{Re_p} & 0.0 \le \tau \le 0.5 \\ \dfrac{Re_s}{Re_p} + \sin[\,2\pi\,(\tau-0.5)\,] & 0.5 \le \tau \le 1.0 \end{cases}\,. \tag{24}$$

In addition to the values of ψ along the walls, the fully developed flow condition on ψ in (20) must be satisfied to insure closure of the Poisson equation. Values of ψ on the left boundary and those on the right boundary are therefore set equivalent.

To calculate $\psi(0,y)$, the values on the left boundary, eqn. (19) needs $\psi(-1,y)$ which does not exist. However, periodicity requires that $\psi(L-1,y)$ be the same as $\psi(-1,y)$ and is applied as such. The stream function on the right boundary is treated similarly.

The boundary conditions in the vorticity equation, (17), require that: 1) the fully developed condition on ω in (20) again be satisfied and 2) a boundary vorticity condition be specified along the solid surfaces. Again using conditions imposed by (21), ω along the solid boundary can be written as

$$\omega_{wall} = \frac{7\ \psi_w - 8\ \psi_{w+1} + \psi_{w+2}}{2\ (\Delta n)^2} \tag{25}$$

where w is the coordinate normal to the wall in the appropriate direction and Δn is the differential spacing in that direction [8]. The problem is now solved except for one remaining difficulty, treatment of the vorticity at the sharp corners protruding into the domain.

Vorticity at a sharp corner such as that shown in Fig. 5a leads to a singularity in the solution since the wall vorticity can be calculated with eqn. (25) in either the x or y direction. Three methods have been tried consisting of: 1) averaging the vorticity as the corner is approached in the x direction with the vorticity as the corner is approached in the y direction, 2) summing these two values of vorticity, and 3) not requiring continuity of vorticity at the corner, i.e. letting the vorticity become a different value when calculated in the x direction than when calculated in the y direction. The latter of the three can be applied since only the derivatives of the vorticity appear in eqn. (9). Instead of requiring continuity around the corner, n in eqn. (25) becomes x for terms containing partial derivatives of ω with respect to the x direction and similarly, n becomes y for terms containing partial derivatives with respect to the y direction. At first glance, eqn. (10) appears to create some difficulty since it depends on the vorticity, not the derivatives of vorticity. However, this equation is not applied along the solid boundaries since ψ is specified there. The three methods yielded identical solutions except in the immediate vicinity of the corners,

which did not seem to significantly affect the flow field. Upon seeing only minor differences between the three, the third method of calculating the wall vorticity in the x direction for terms containing partial derivatives with respect to x and applying a similar procedure to terms containing partial derivatives with respect to y, is used in all solutions based on the recommendations in [8].

As the calculation starts from $\tau = 0.000$, all values of ω and ψ are initialized to zero. Beginning with the first step in time, the flowrate, as well as the other boundary conditions are applied. At this first step, $\tau = 0.001$, eqn. (17) requires information from two prior time steps, of which only one exists. This problem is dealt with by using the initial information for both of the required time steps.

At each time index, n+1, the procedure first calculates the interior vorticity field using information on ψ at n and information on ω at n and n-1. Boundary values of ψ are then introduced which are dependent on the time within the cycle, τ. Eqn. (19) is then solved iteratively for the interior ψ field using the most recent information on ω, that from time n+1,until the convergence criteria of the maximum variation in ψ is less than 1×10^{-4}, as discussed above. Lastly, the wall vorticity is calculated from eqn. (25), once again using the most recent ψ values at time n+1. This is repeated for each of the one thousand time steps in a cycle. To rid the calculations of the initial condition of zero flow everywhere, the solution proceeds in time for several full cycles until no variation from cycle to cycle is seen.

Initial calculations with a mesh size of 42 x 34 grid spacings in the x and y directions produce solutions with good experimental agreement in all but a few of the cases studied. In these cases, where Re_s and Re_p are high, oscillations occur in the vorticity field near the downstream protruding corner. A finer resolution mesh of 84 x 68 (shown in Fig. 5b) resolved this problem and no further oscillations have been

observed. With the exception of the cases where there are oscillations at the impingement corner, solutions on a 84 x 68 mesh matched those on a 42 x 34 mesh.

To reduce the CPU time used in the calculations, the 84 x 68 mesh is not used from the initial no-flow conditions. Instead, the solution starts with a 42 x 34 mesh and is developed from no-flow through three full cycles, which is 3000 time steps. The solution at the end of three cycles is is then linearly interpolated onto a 84 x 68 mesh and used as the *initial* condition for the 84 x 68 mesh. The fine mesh solution is developed for another three full cycles to eliminate initial condition effects. All results in this study have been developed for at least 6000 steps in time, consisting of three cycles using the 42 x 34 mesh and then three subsequent cycles using the 84 x 68 mesh.

Discussion of Results-

In this section, the structure of the unsteady fluid motion as a function of the defining parameters is discussed and an explanation is given for how improved interaction with trapped cavity fluid can be achieved. Before any results of time dependent motion are shown, steady flow experimental and numerical results for $Re_s = 120$ are compared (see Fig. 6). Identical fluid behavior in the experiments and numerical solutions is apparent when the particle pathlines are compared with the numerically calculated streamlines. The vortex position within the cavity is the same and there is extremely good agreement where the particle pathlines and streamlines change direction quickly. Closer inspection of the experimental photograph in Fig. 6a also shows that the shear layer recedes slightly into the cavity in the vicinity of the attachment points at the cavity corners; this is also shown in the calculated streamlines plotted in Fig. 6b where positive values of the stream function are shown as solid lines and negative values are shown as dashed lines. Figure 6c, which shows a plot of the vorticity contours for $Re_s = 120$, suggests that the cavity, specifically, the corners of the cavity, influence the fluid motion out to roughly one-fourth of the channel width into the mainstream. However, Figs. 6a and 6b show that little effect is felt on the streamlines and particle pathlines aside from the relaxation of the no-slip condition over the length of the cavity-mainstream interface. The recirculatory fluid within the cavity is driven by the mainstream but appears to have very little interaction across the shear layer. Velocities encountered within the cavity are much lower that those in the mainstream. The maximum value of the stream function is 4% of that in the mainstream, i.e. the flow rate in the cavity is on the order of 4% of the mainstream flow rate.

Detailed study of the time dependent motion with a velocity profile similar to that shown in Fig. 2, over the range of parameters of $0 \leq Re_s \leq 120$, $0.10 \leq S_t \leq 0.50$, and $0 \leq F_p \leq 40$ shows that the fluid motion can be characterized into one of two types. The criterion used for classification is whether the shear layer, which separates the cavity from the mainstream in steady flow, remains intact throughout an entire cycle. Points in the Re_s, S_t, and F_p parameter space where the shear layer is present at all times in a cycle are said to exhibit *sloshing* mode behavior. The fluid motion in this mode is similar to steady flow and thus has the same drawbacks of steady flow. If, at some point in the cycle, the shear layer is severed by mainstream fluid entering the cavity, a *mixing* mode cycle is said to be present. In this mode there is stronger interaction between the mainstream and cavity fluid than there is in the *sloshing* mode.

In the *sloshing* mode, a well defined vortex remains in the cavity throughout the cycle. Although the shear layer is always present in this mode, its position shifts during the cycle. Figure 7a,b shows numerically calculated streamlines for a full cycle of a typical *sloshing* mode, and Fig. 8a,b shows the experimentally obtained particle pathlines for the same case. Notice that for $0.3 \leq \tau \leq 0.5$, the fluid motion within the cavity and in the mainstream is similar to the steady flow shown in Fig. 6a,b. During the period $0.5 \leq \tau \leq 0.75$, the accelerating mainstream fluid displaces the shear layer into the cavity and for a short time the center of the vortex is shifted toward the upstream half of the cavity. As the motion starts to decelerate at $\tau = 0.75$ down to where it reaches steady flow at $\tau = 1.0$, the center of the vortex moves back to its original position and the vortex grows in size, expanding slightly into the mainstream. This growth in size of the vortex during deceleration is not uncommon and has been shown in [1,2,3]. Returning to the steady half cycle, the streamlines for $0.0 \leq \tau \leq 0.2$, show that the motion does not instantly settle down to steady flow, but instead some

adjustment time is needed to recover from the previous pulse. The streamlines, however, appear similar to those resulting from steady forcing by $\tau = 0.3$.

The *sloshing* mode is similar to steady flow because the forcing function which drives the fluid motion has a weak pulsatile component and a relatively strong steady component. In the experiments, the pulsatile component depends on the piston displacement and on the frequency of oscillation of the piston. Weak pulsatile conditions, which yield a small Re_p, result from a relatively small piston displacement, a low frequency of oscillation, or a combination of both. As implied when the dimensionless parameters were defined, the ratio of Re_p to Re_s is a strong indication of the characteristics of the fluid motion. For the sloshing case shown in Fig. 7a,b and Fig. 8a,b, $\frac{Re_p}{Re_s} = 0.56$, thus the peak pulsatile Reynolds number is only a fraction of the steady Reynolds number. In the numerical calculations, this ratio affects the driving mechanism through the boundary conditions imposed on ψ. In eqn. (24), the steady forcing component is the inverse of $\frac{Re_p}{Re_s}$, and the pulsatile component is expressed by the sine term. For the case in Figs. 7a,b and 8a,b, the magnitude of the steady term is $\frac{1}{0.56} = 1.79$ and the maximum value of the sine term is 1.0 at $\tau = 0.75$. Since the steady term is always much larger than the time dependent term, the steady component controls the flow structure and the *sloshing* mode appears similar to steady forcing.

The *mixing* mode is quite different from the sloshing mode. During a cycle in the *mixing* mode, the shear layer spanning the cavity does not remain intact throughout a cycle. Figure 9a,b shows numerically calculated instantaneous streamlines for a full cycle of a typical *mixing* mode, while Fig. 10a,b shows the particle pathlines for the same cycle. In the first half cycle, where only a steady forcing function is present, the fluid in the cavity undergoes an adjustment period following the preceding cycle,

similar to that shown in a *sloshing* mode. A full recovery to a steady flow solution is not possible, however, before the pulsatile motion of the second half cycle starts at $\tau = 0.5$.

The acceleration and subsequent deceleration in the second half cycle in a *mixing* mode forces interaction of the mainstream with the cavity fluid. As the accelerating mainstream encounters the sudden expansion of the cavity, fluid swirls around the upstream corner of the cavity, severing the shear layer. This process occurs between $\tau = 0.5$ and $\tau = 0.6$ since at $\tau = 0.6$ in Fig. 9b, the separation streamline does not exist and in Fig. 10b, the movement of fluid into the cavity is very noticeable. As mainstream fluid enters the cavity, it simultaneously destroys the vortex by forcing this fluid out of the cavity and forms a new vortex from the swirling motion at the upstream cavity corner. As the deceleration begins at $\tau = 0.75$, the new vortex grows to fill the cavity and shift its center downstream. Growth of the vortex increases until it protrudes significantly into the mainstream shown at $\tau = 1.0$ in Fig. 9b, when the forcing function returns to steady conditions.

For the *mixing* case shown in Figs. 9a,b and 10a,b, the ratio of $\frac{Re_p}{Re_s} = 0.91$, so the magnitude of Re_p is approximately the same as the magnitude of Re_s. In eqn. (24), the steady forcing component has a magnitude of $\frac{1}{0.91} = 1.10$ which is comparable to the maximum value of the sine term.

The transition from *sloshing* to *mixing* is a strong function of $\frac{Re_p}{Re_s}$. For $\frac{Re_p}{Re_s}$ near zero, the fluid motion is essentially steady with no noticeable change in flow characteristics in a cycle. Small values of the ratio yields *sloshing* behavior of the cavity fluid. Forcing functions with $\frac{Re_p}{Re_s}$ near 1.0 mark the division between *sloshing*

modes and *mixing* modes with higher values operating in a *mixing* mode. Large values of $\frac{Re_p}{Re_s}$ characterize strong *mixing* of the fluid.

In every Re_s = constant plane in parameter space, there is a locus of (F_p, S_t) points that separate the *sloshing* mode from the *mixing* mode. For the $Re_s = 120$ plane, a plot of F_p versus S_t in Fig. 11 shows a linear relationship. Operating points above the *sloshing/mixing* line are in the *mixing* mode while points below are in the *sloshing* mode. By definition

$$Re_p = \frac{F_p}{S_t},$$

so the value of Re_p at any point on the *sloshing/mixing* line can be found by drawing a ray from the origin. Since the *sloshing/mixing* line does not intersect the origin $\frac{Re_p}{Re_s}$ decreases weakly with increasing S_t. However, since $\frac{Re_p}{Re_s}$ is approximately constant, this ratio makes an excellent means of comparing the relative behavior of two flows at $Re_s = 120$.

In Fig. 12, *sloshing/mixing* lines are plotted as a function of F_p and S_t for three different values of Re_s. Each line is approximately linear, indicating that as S_t increases, F_p also increases. Starting at a point in the *sloshing* regime for $Re_s = 120$, the *mixing* mode can be reached by either increasing F_p, decreasing S_t, or decreasing Re_s. Starting at a point in the *mixing* regime, as Re_s increases, Re_p must also increase to maintain *mixing* behavior.

Instantaneous streamlines for an excellent mixing case are shown in Fig. 13a,b and the corresponding experimentally obtained particle pathlines are shown in Fig. 14a,b. The parameters in these figures are: $Re_s = 42$, $F_p = 26.3$, and $S_t = 0.147$, so

$Re_p = 179$. The pulsatile/steady ratio is $\frac{Re_p}{Re_s} = 4.3$, which means there is extremely strong mixing. Comparing the numerical results of Fig. 13a,b with the experimental results of Fig. 14a,b, shows excellent agreement between the particle pathlines and the instantaneous streamlines. During the first half of the cycle (the steady half cycle), the vortex in the cavity is large and strong, and only a small portion of it dissipates before the next driving pulse at $\tau = 0.5$. During acceleration, $0.5 \leq \tau \leq 0.75$, mainstream fluid enters the cavity near the upstream corner and simultaneously washes out the existing vortex in a manner that is similar to the weaker *mixing* case discussed before. At $\tau = 0.70$, a new vortex can be seen forming near the upstream corner. During the deceleration, the new vortex grows to completely fill the cavity and its center shifts downstream. As the steady half cycle begins, careful examination of the streamlines show that the vortex is now so strong that fluid is driven *back upstream* slightly around the upstream corner. Other indications of the vortex strength are the large displacement of the streamlines in the channel and the recirculatory regions on the *opposite* flat wall. Since these recirculation regions are periodically washed downstream, the presence of these regions help the mixing process. Thus, as expected, a high $\frac{Re_p}{Re_s}$ value yields an excellent mixing case which exhibits an extremely strong cavity vortex.

Conclusions-

Up to a steady Reynolds number of $Re_s = 120$, the numerical results presented here are assumed accurate as experimentally obtained particle pathlines and numerically calculated instantaneous streamlines correspond closely. The ability of the finite difference code to accurately define the flow conditions has been tested and shown to be valid over the range of parameters $0 \le Re_s \le 120$, $0.10 \le S_t \le 0.50$, and $0 \le F_p \le 40$.

Periodic fluid motion of the type described in this study can be categorized as operating in one of two modes: a sloshing mode, or a mixing mode; the distinction being whether the shear layer spanning the cavity is severed at some point in the cycle, showing cavity-mainstream interaction aside from the mainstream merely driving the cavity flow through the shear layer. For a specific Re_s, an operating region can be mapped out for each of the two modes. A plot of these regions shows an almost linear relationship between the frequency parameter, F_p, and the Strouhal number, S_t. Starting from a point in the *sloshing* regime, transition to *mixing* mode behavior can be achieved by increasing F_p, decreasing S_t, or decreasing Re_s.

Excellent cavity mixing is achieved by selectively choosing the operating point for a given Re_S such that the ratio of $\frac{Re_p}{Re_s}$ is sufficiently larger than that necessary to cause mixing. It is postulated that the best operating points on a plot such as that shown in Fig. 12 are those that are in a direction perpendicular (upwards and to the left) to the sloshing/mixing line for a given Re_s since this yields a large value of $\frac{Re_p}{Re_s}$.

Proposed Research-

Enhanced heat transfer in flow past a series of rectangular cavities can be achieved by increased mixing between the mainstream and the cavities. A method has been presented to promote fluid mixing between the two regions. To determine the effectiveness of the method in enhancing heat transfer from the separated regions, experimental and numerical modeling will be developed to include heat transfer from the surfaces which bound the cavity in the present study.

In the experimental channel, the heat transfer surfaces will be supplied with constant heat flux sources and temperature measurements from these surfaces and from within the fluid will yield a means of determining an overall heat transfer coefficient. Measurement of the bulk fluid temperature as a function of axial position through the heated test section will provide the amount of heat transfer to the fluid and also provide correlations for the boundary conditions in the numerical simulation.

The numerical solutions for the flow structure will be developed to include a finite difference approximation to the energy equation. This equation, which can be solved subsequent to the fluid flow solution, will use experimental data to impose the temperature boundary conditions in the solutions. Once the energy equation is solved, the temperature field throughout the fluid can be found at any time in a cycle under the forcing functions described in this thesis. By numerical integration, an average heat transfer coefficient will then be found which is a function of the forcing parameters. The heat transfer coefficient is the factor necessary to compare the convection characteristics of different flows. This will yield a measure of the effects of using pulsatile components superimposed on steady flow in comparison to pure steady flow.

Figure Captions-

Figure 1 Cross-section of experimental test section and model of numerical method. Flow is planar past a series of rectangular cavities located on one wall only.

Figure 2 Mean velocity U(t). The cyclic velocity consists of a steady velocity, U_s for $0 \leq \tau \leq 0.5$, and a velocity U_s plus a sinusoidal acceleration and deceleration of amplitude U_p for $0.5 \leq \tau \leq 1.0$.

Figure 3 Schematic drawing of the experimental channel. Flow enters from the left through the diffuser and then travels down a long flow straightening section before reaching the middle test section. After exiting the test section it passes through another long, flat section before converging down to the exit piping.

Figure 4 Inlet flow schematic. The pulsatile flow component is supplied through one-way valve A while a constant head steady flow component is supplied through one-way valve B. Drawing fluid through valve A, the oscillating piston determines the quantity and frequency of the added pulsatile component which is expelled through one-way valve C.

Figure 5 a) Definition of cavity dimensions. (h-channel width, d-cavity depth, l-cavity length, L-geometric periodicity length).

b) Mesh of numerical solutions, 84 x 68 grid spacings in the axial and transverse directions.

Figure 6 a) Particle pathlines of steady flow at $Re_s = 120$.

b) Numerically calculated streamlines at $Re_s = 120$.

c) Numerically calculated vorticity contours at $Re_s = 120$.

Figure 7 a) Streamlines showing sloshing mode for $0 \leq \tau \leq 0.5$.

($Re_s = 120$, $F_p = 13.2$, $S_t = 0.197$)

b) Streamlines showing sloshing mode for $0.5 \leq \tau \leq 1.0$.

($Re_s = 120$, $F_p = 13.2$, $S_t = 0.197$)

Figure 8 a) Particle pathlines showing sloshing mode for $0 \leq \tau \leq 0.5$.

($Re_s = 120$, $F_p = 13.2$, $S_t = 0.197$).

b) Particle pathlines showing sloshing mode for $0.5 \leq \tau \leq 1.0$.

($Re_s = 120$, $F_p = 13.2$, $S_t = 0.197$).

Figure 9 a) Streamlines showing mixing mode for $0 \leq \tau \leq 0.5$.

($Re_s = 120$, $F_p = 26.3$, $S_t = 0.241$)

b) Streamlines showing mixing mode for $0.5 \leq \tau \leq 1.0$.

($Re_s = 120$, $F_p = 26.3$, $S_t = 0.241$)

Figure 10 a) Particle pathlines showing mixing mode for $0 \leq \tau \leq 0.5$.

($Re_s = 120$, $F_p = 26.3$, $S_t = 0.241$).

b) Particle pathlines showing mixing mode for $0.5 \leq \tau \leq 1.0$.

($Re_s = 120$, $F_p = 26.3$, $S_t = 0.241$).

Figure 11 Plot of F_p vs. S_t showing the dividing lines between the sloshing and mixing modes ($Re_s = 120$). Mixing modes exist above, while sloshing modes exist below the sloshing/mixing line.

Figure 12 Plot of F_p vs. S_t showing the dividing lines between the sloshing and mixing modes as a function of Re_s ($Re_s = 50, 90, 120$).

Figure 13 a) Streamlines showing excellent mixing for $0 \leq \tau \leq 0.5$.

($Re_s = 42$, $F_p = 26.3$, $S_t = 0.147$)

b) Streamlines showing excellent mixing for $0.5 \leq \tau \leq 1.0$.

($Re_s = 42$, $F_p = 26.3$, $S_t = 0.147$)

Figure 14 a) Particle pathlines showing excellent mixing for $0 \leq \tau \leq 0.5$.

($Re_s = 42$, $F_p = 26.3$, $S_t = 0.147$)

b) Particle pathlines showing excellent mixing for $0.5 \leq \tau \leq 1.0$.

($Re_s = 42$, $F_p = 26.3$, $S_t = 0.147$)

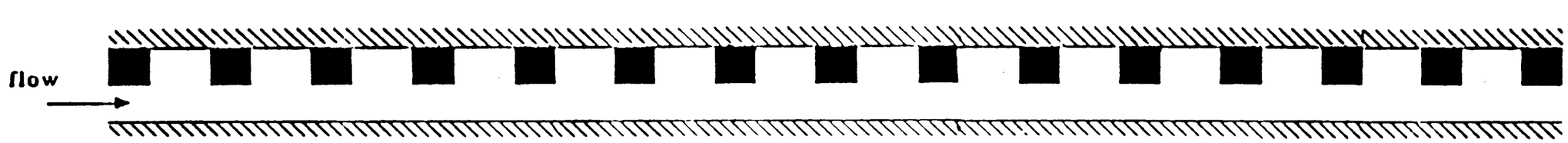

Figure 1

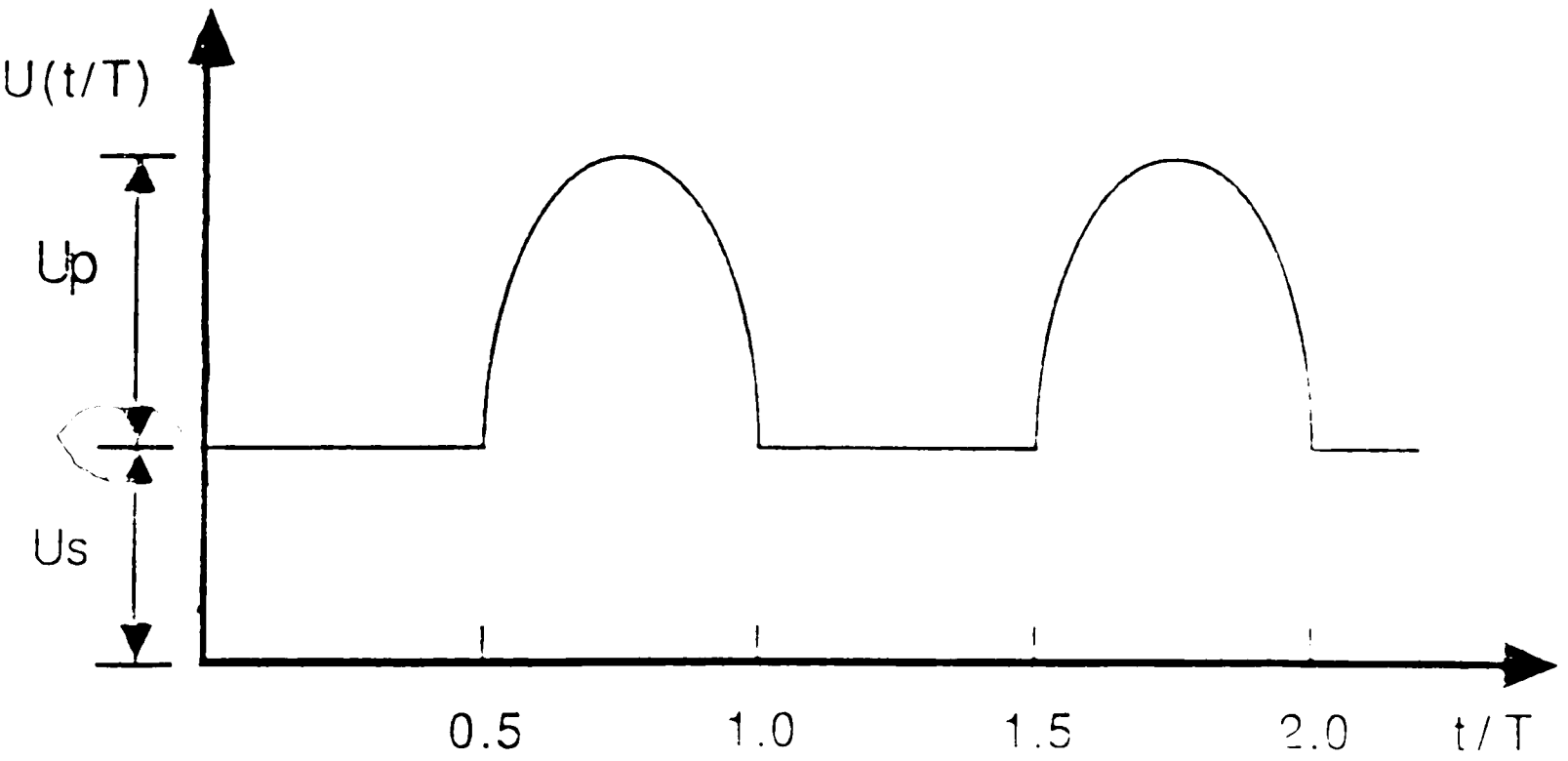

U_p - amplitude of pulsatile velocity

U_s - steady velocity

T - period of forcing function

Figure 2

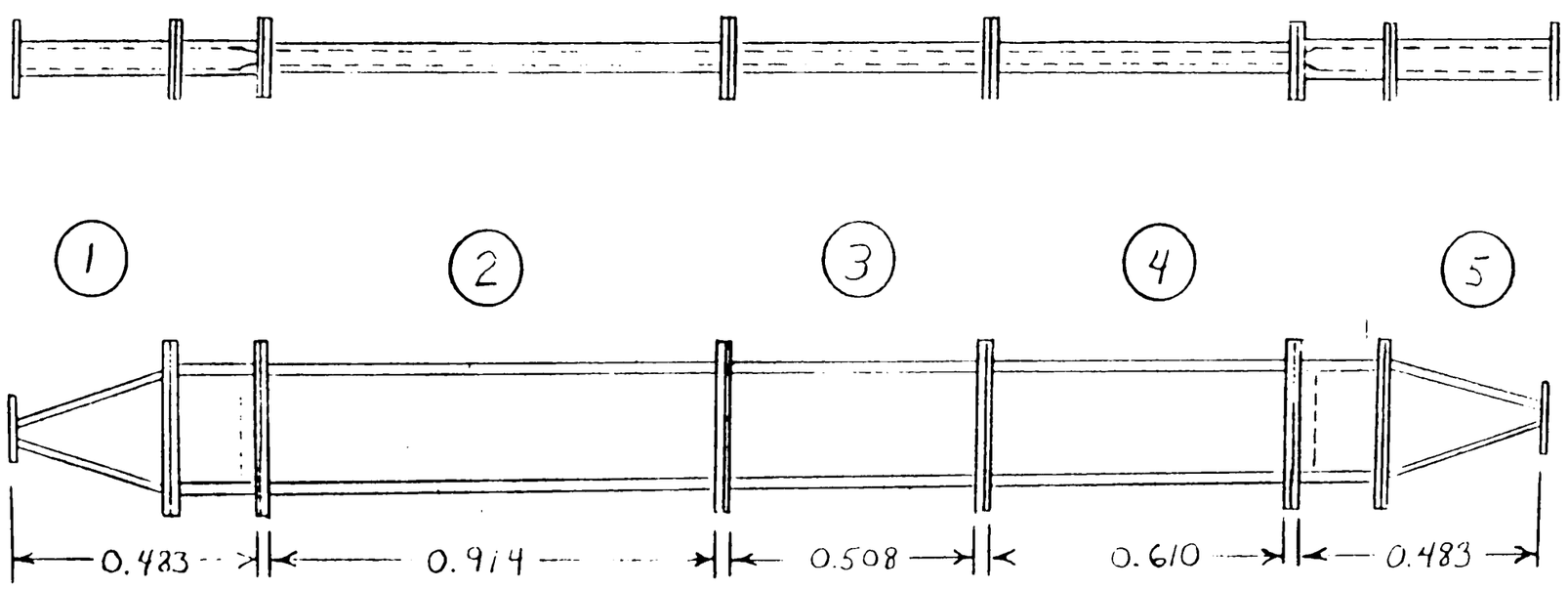

Figure 3

(1) DIFFUSER SECTION
(2) UPSTREAM FLAT WALL
(3) TEST SECTION
(4) DOWNSTREAM FLAT WALL
(5) CONVERGENT SECTION

ALL DIMENSIONS IN METERS
SCALE = $\frac{1}{20}$

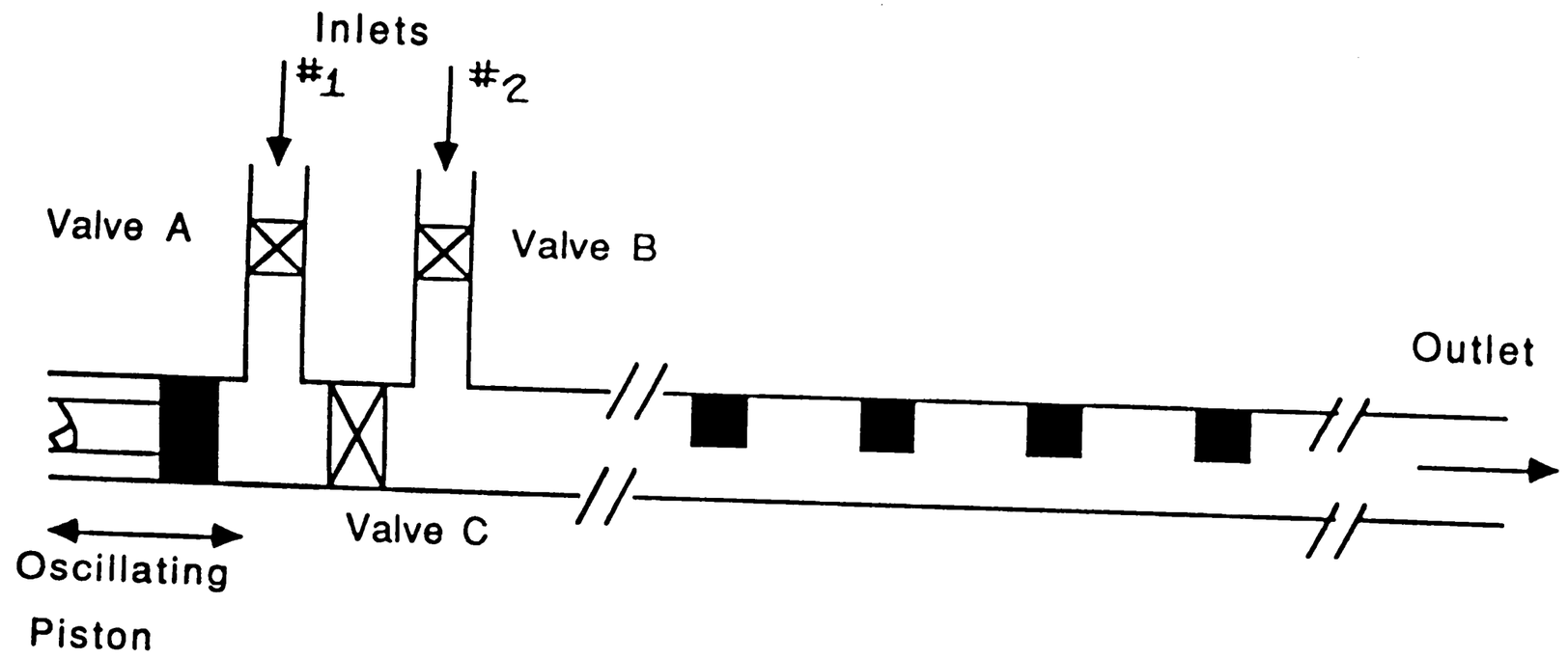

Figure 4

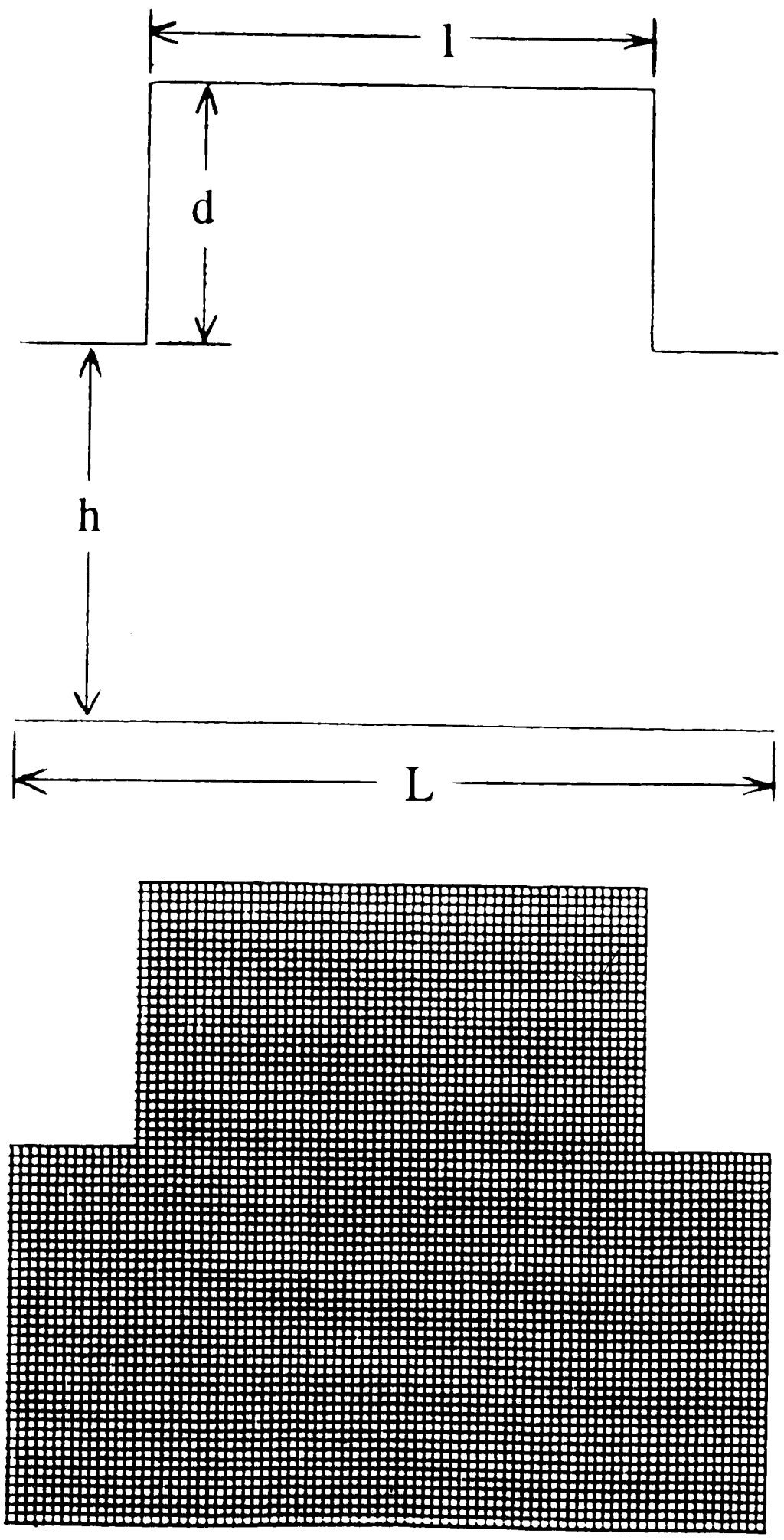

(a)

(b)

Figure 5

(a)

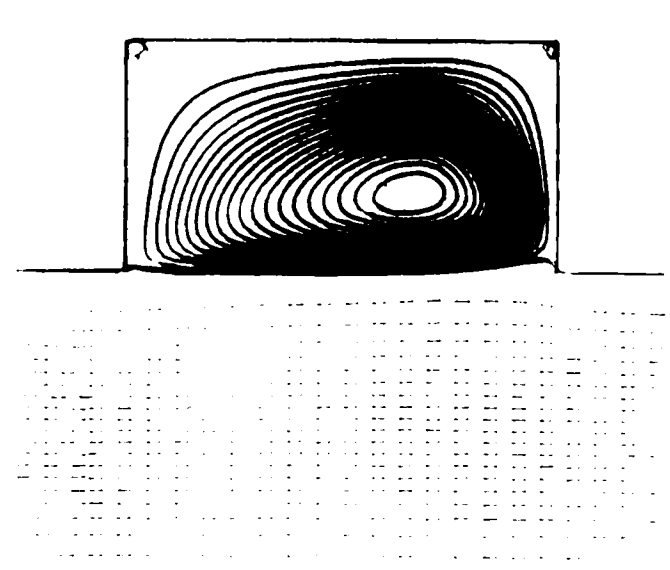

(b)

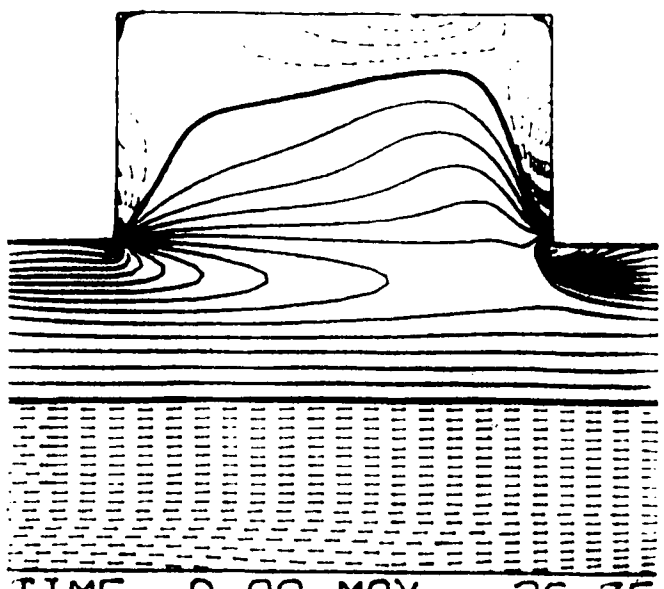

(c)

Figure 6

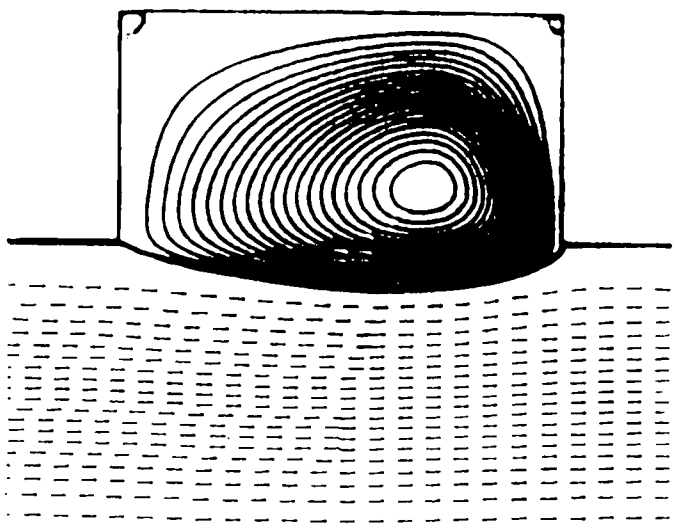

TIME= 6.00 MAX= .20
MIN= -1.79

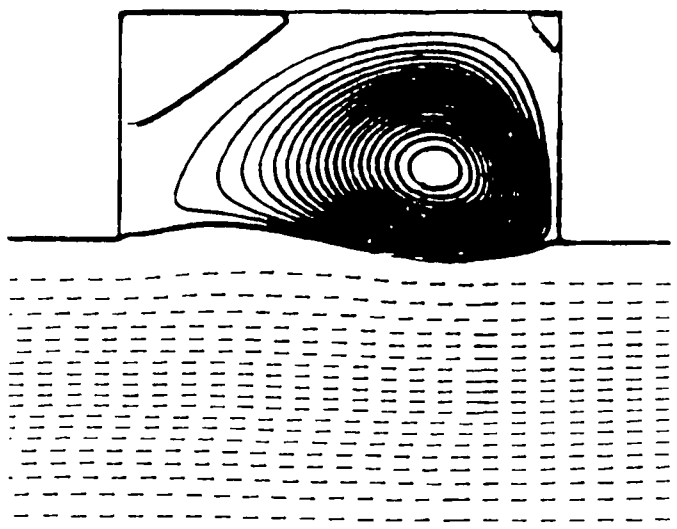

TIME= 6.10 MAX= .12
MIN= -1.79

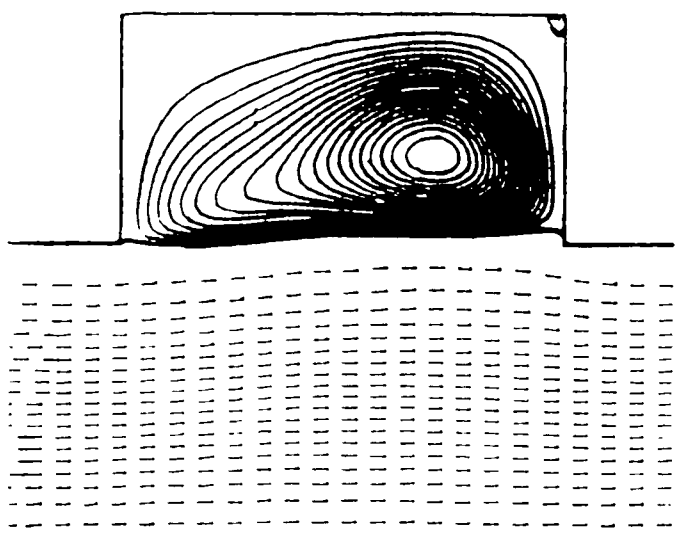

TIME= 6.20 MAX= .07
MIN= -1.79

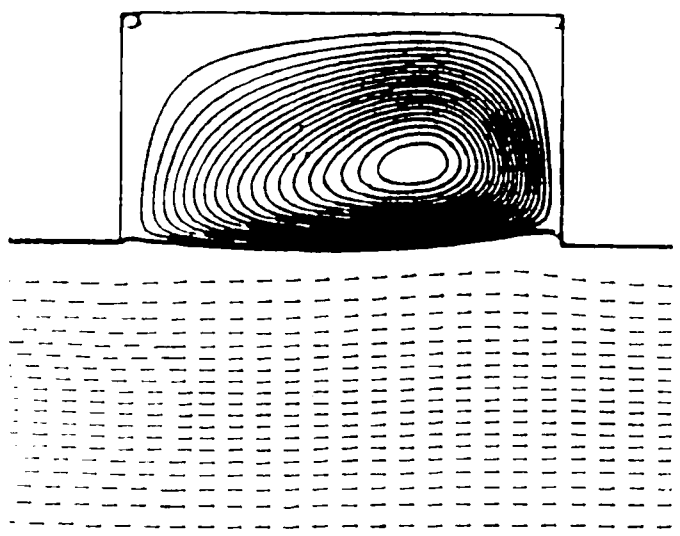

TIME= 6.30 MAX= .08
MIN= -1.79

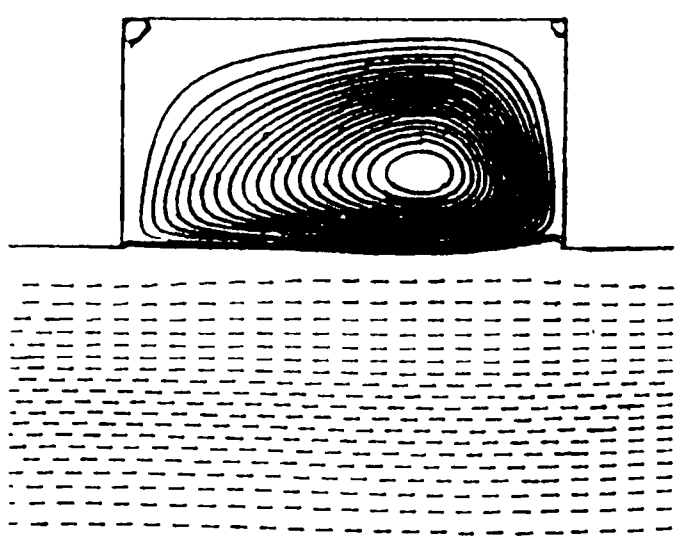

TIME= 6.40 MAX= .07
MIN= -1.79

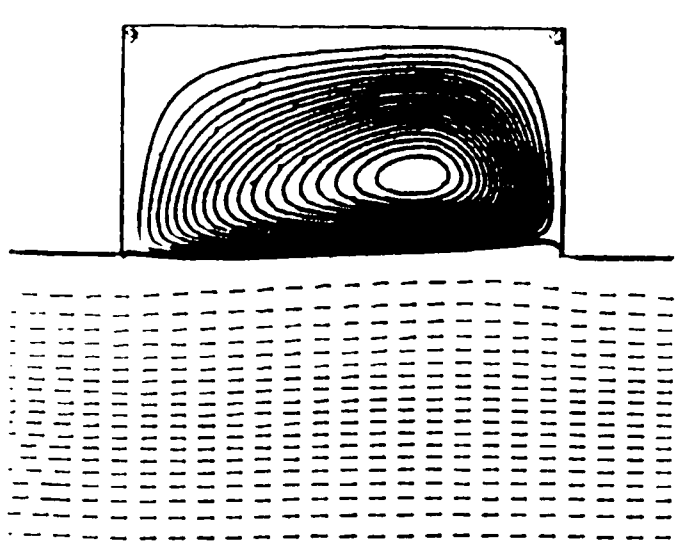

TIME= 6.50 MAX= .06
MIN= -1.79

Figure 7a

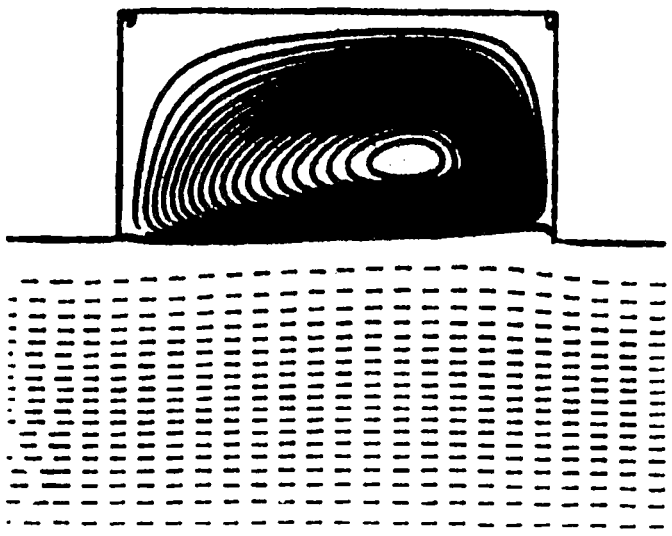

TIME- 6.50 MAX- .06
MIN- -1.79

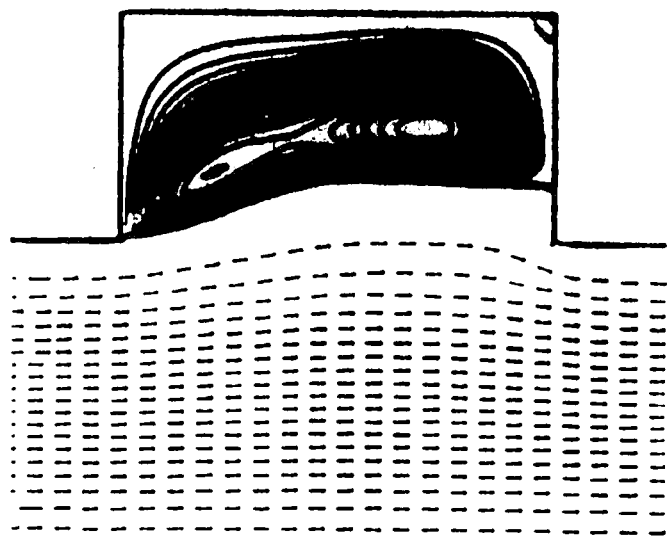

TIME- 6.60 MAX- .02
MIN- -2.38

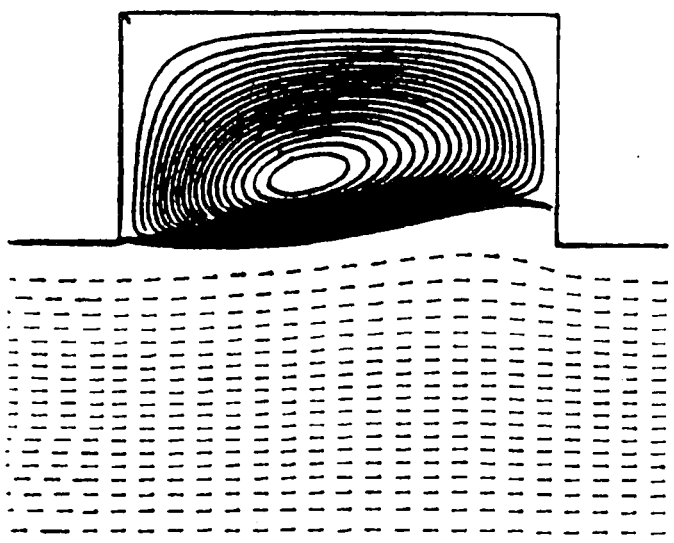

TIME- 6.70 MAX- .08
MIN- -2.74

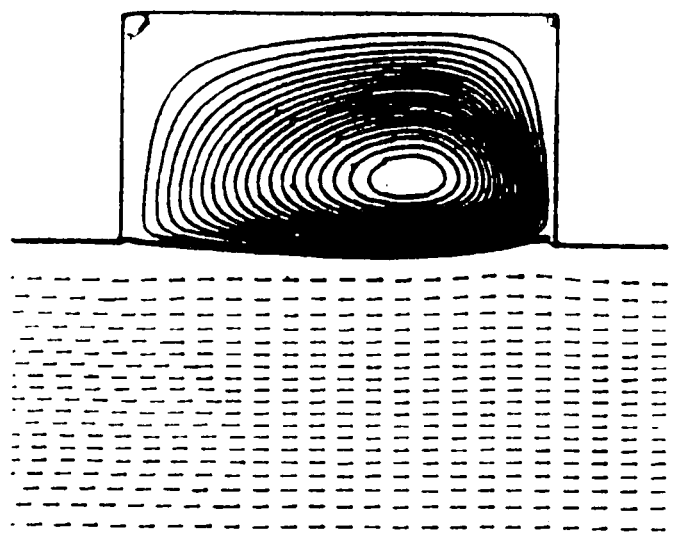

TIME- 6.80 MAX- .14
MIN- -2.74

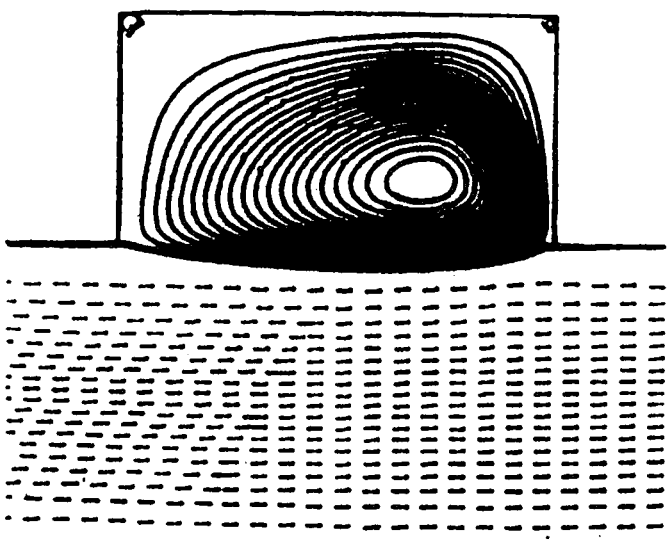

TIME- 6.90 MAX- .17
MIN- -2.38

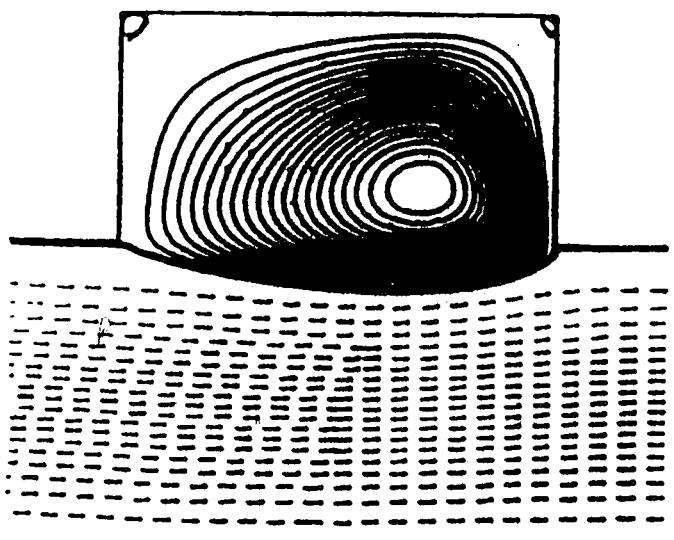

TIME- 7.00 MAX- .20
MIN- -1.79

Figure 7b

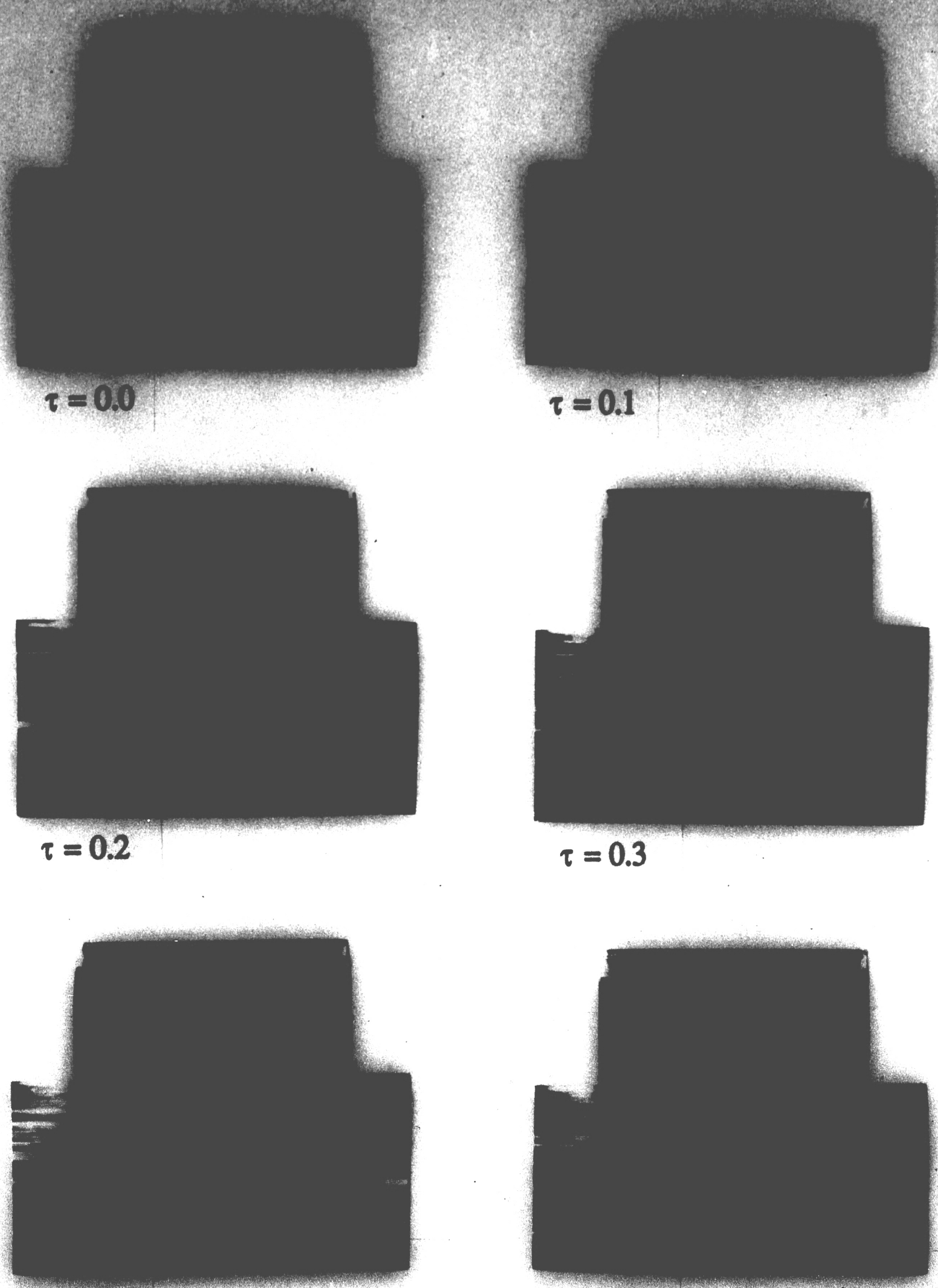

Figure 8a

$\tau = 0.5$

$\tau = 0.6$

$\tau = 0.7$

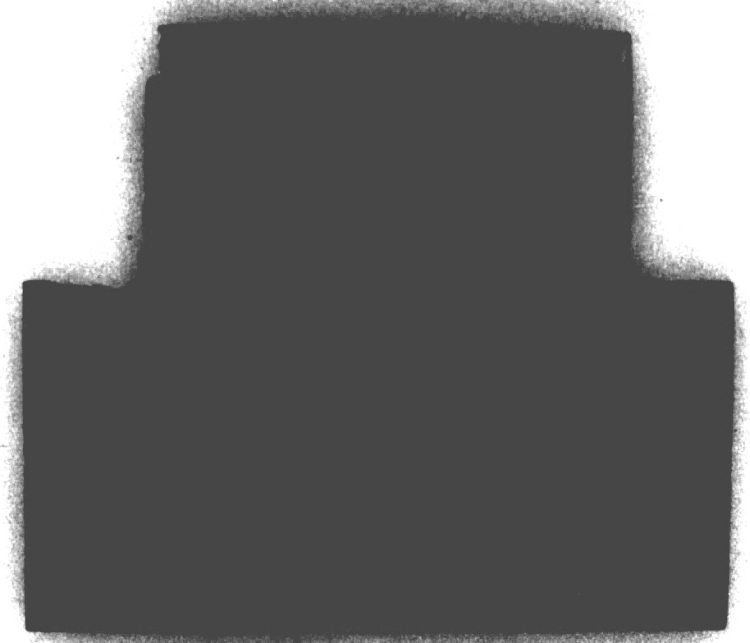

$\tau = 0.8$

$\tau = 0.9$

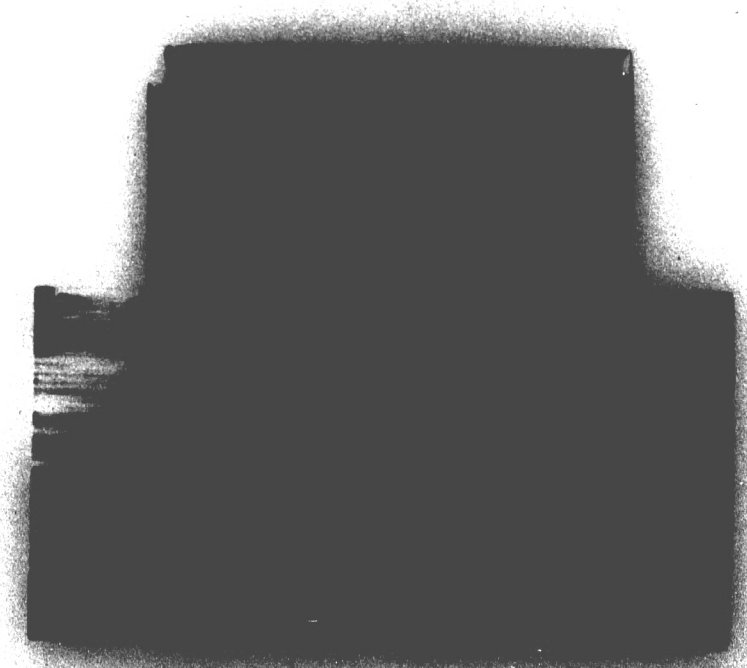

$\tau = 1.0$

Figure 8b

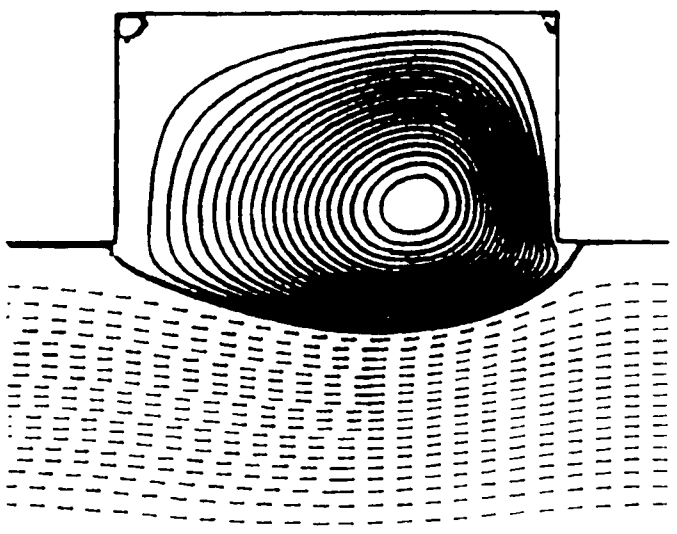

TIME= 6.00 MAX= .31
MIN= -1.10

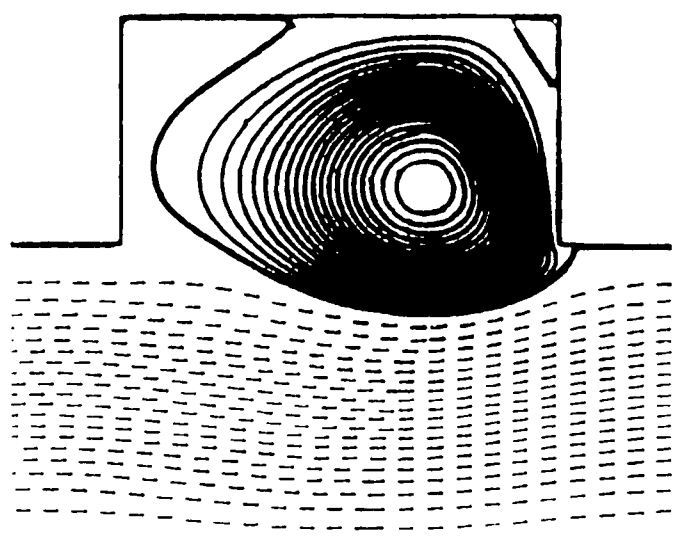

TIME= 6.10 MAX= .25
MIN= -1.10

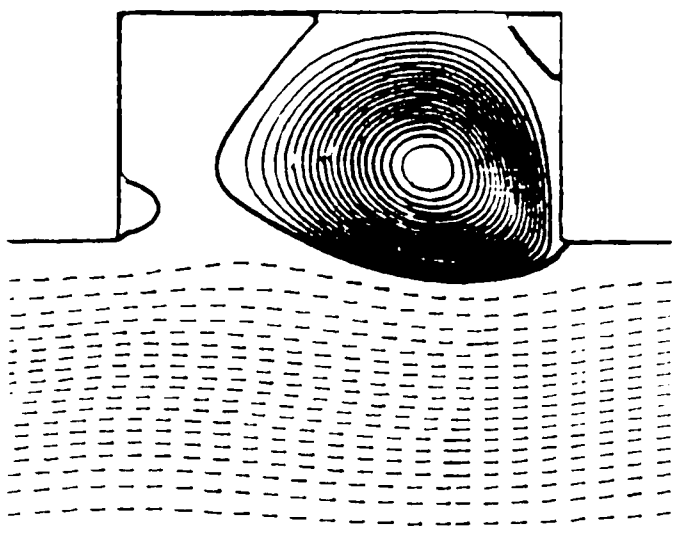

TIME= 6.20 MAX= .18
MIN= -1.10

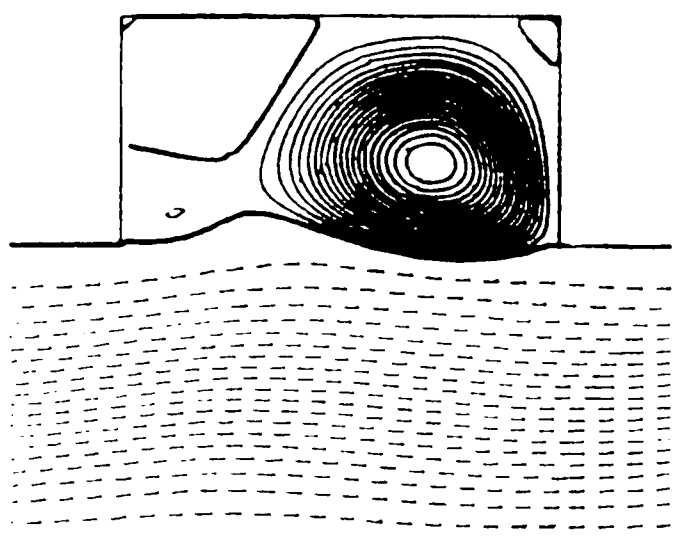

TIME= 6.30 MAX= .13
MIN= -1.10

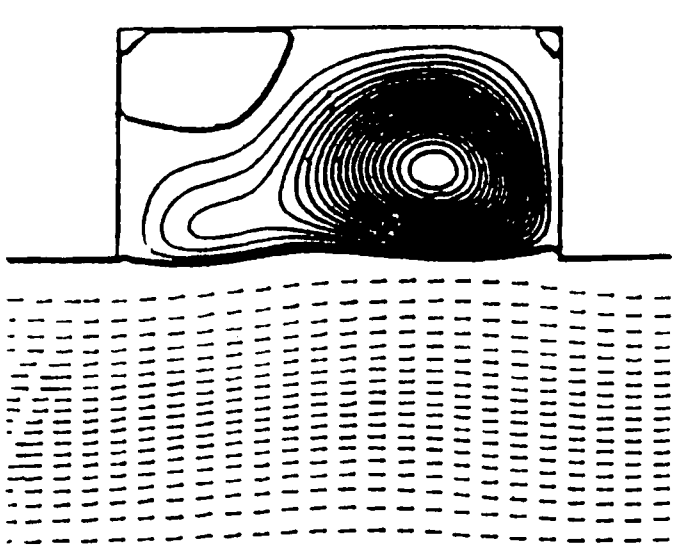

TIME= 6.40 MAX= .10
MIN= -1.10

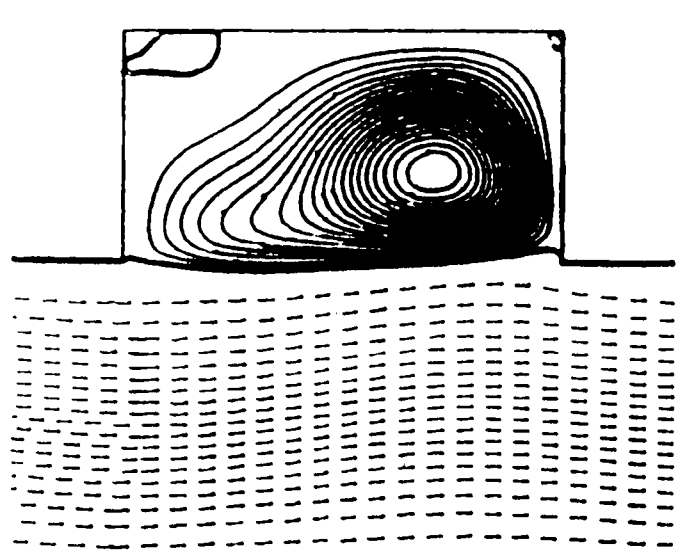

TIME= 6.50 MAX= .09
MIN= -1.10

Figure 9a

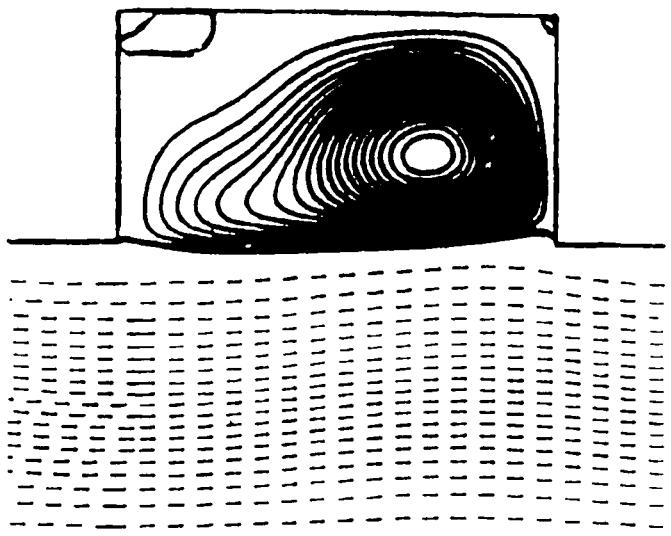

TIME= 6.50 MAX= .09
MIN= -1.10

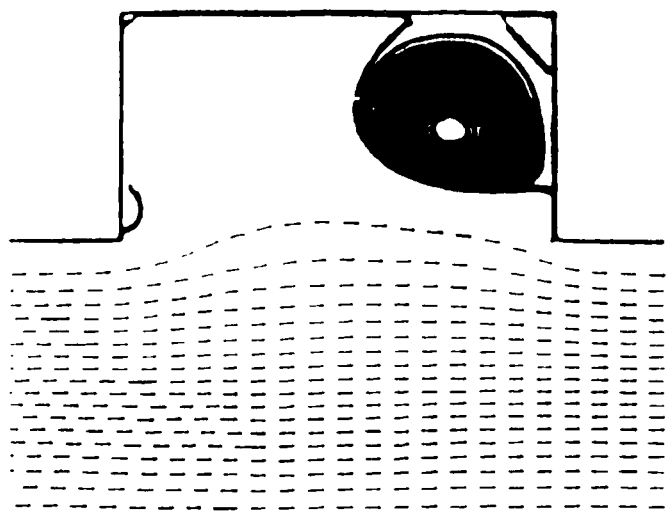

TIME= 6.60 MAX= .03
MIN= -1.69

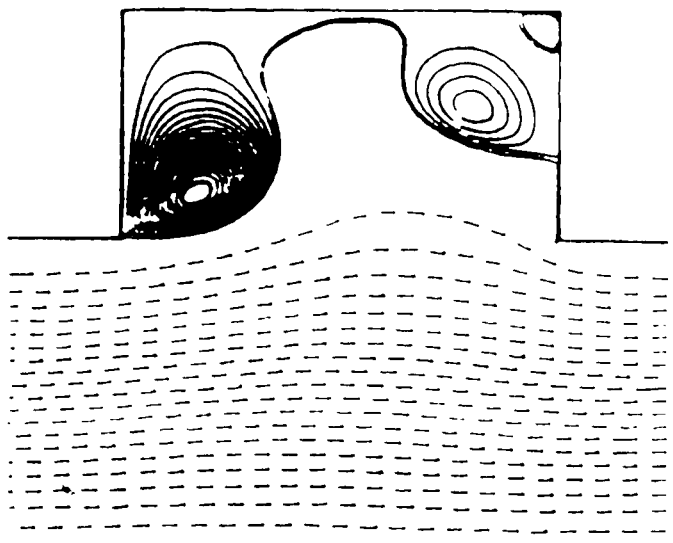

TIME= 6.70 MAX= .03
MIN= -2.05

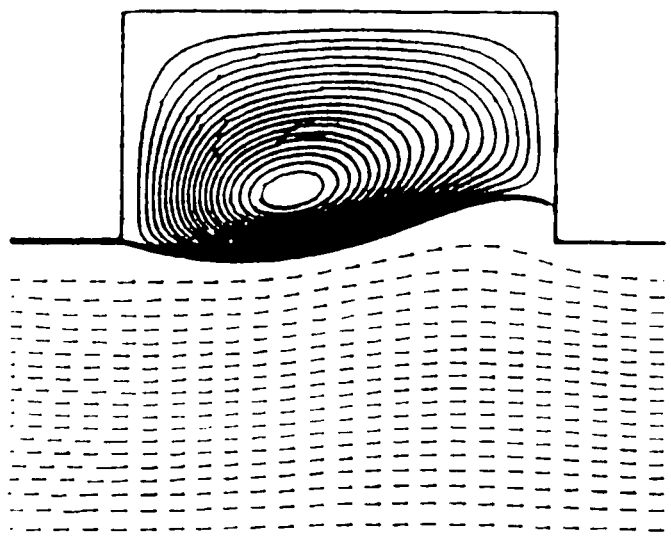

TIME= 6.80 MAX= .12
MIN= -2.05

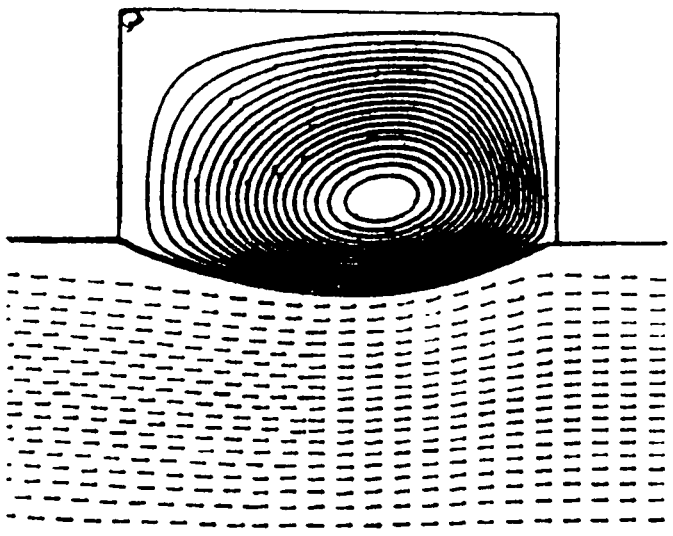

TIME= 6.90 MAX= .24
MIN= -1.69

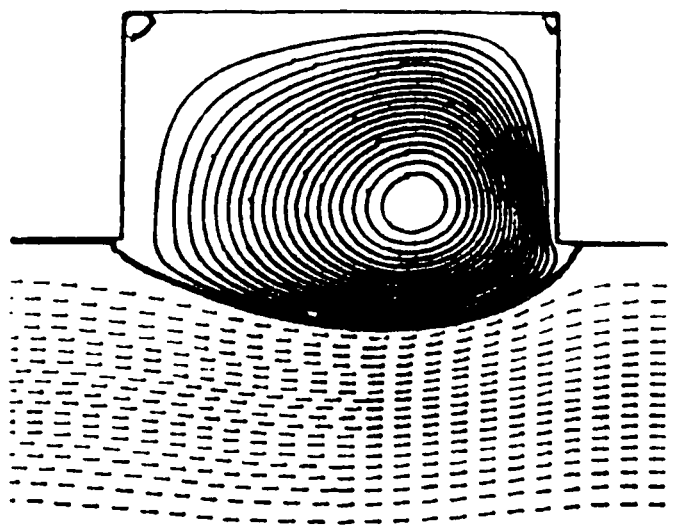

TIME= 7.00 MAX= .31
MIN= -1.10

Figure 9b

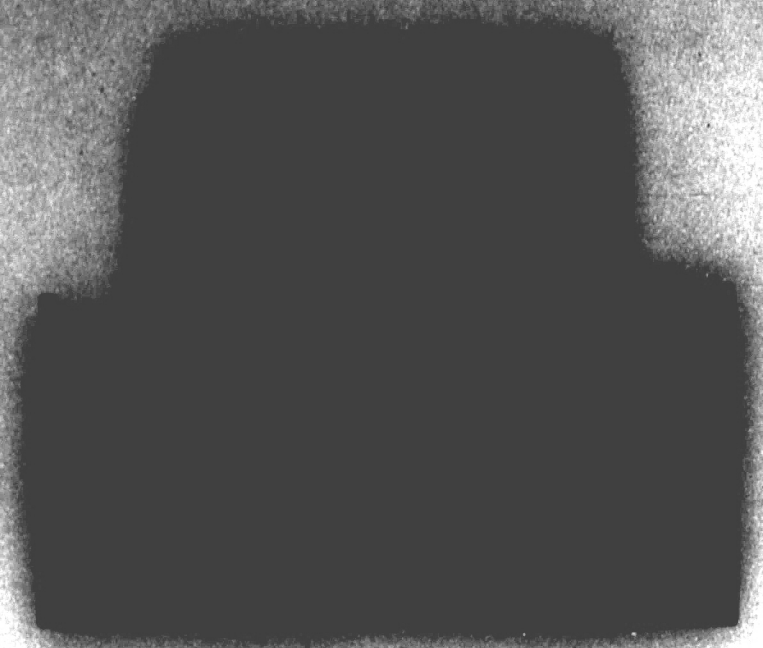

$\tau = 0.0$

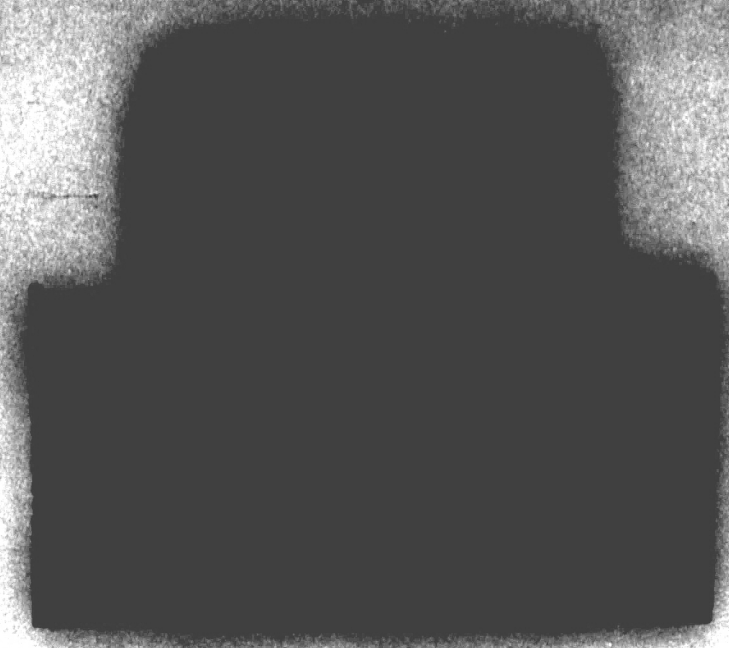

$\tau = 0.1$

$\tau = 0.2$

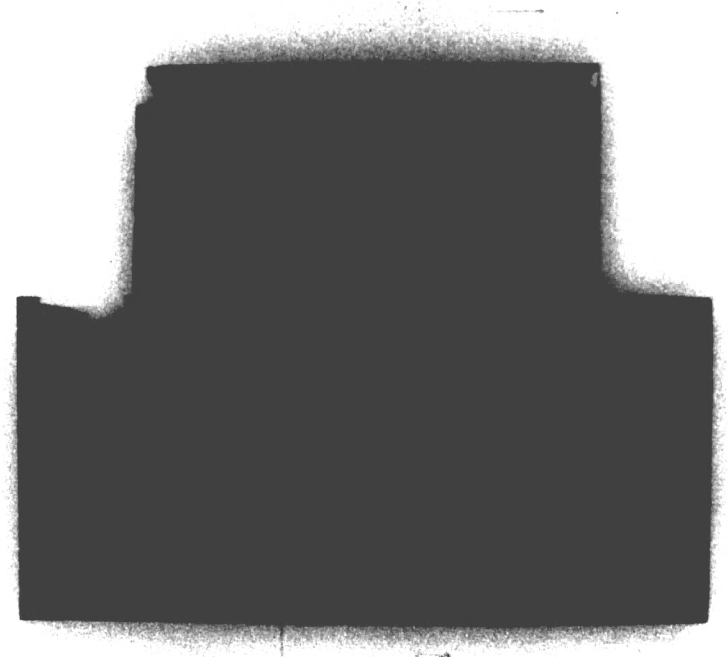

$\tau = 0.3$

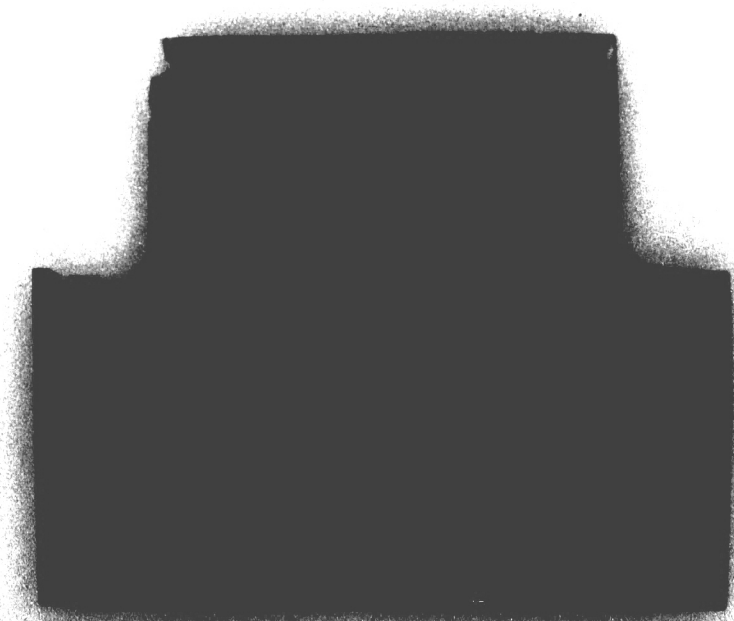

$\tau = 0.4$

$\tau = 0.5$

Figure 10a

$\tau = 0.5$

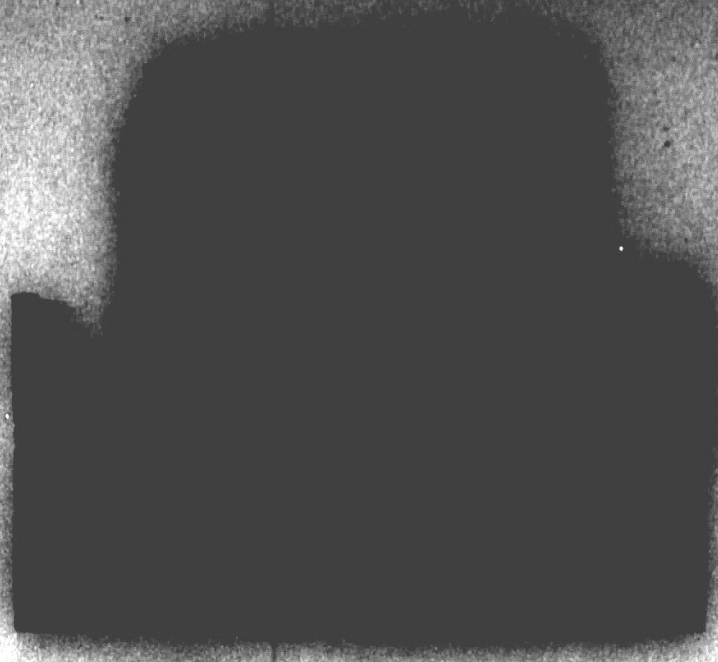

$\tau = 0.6$

$\tau = 0.7$

$\tau = 0.8$

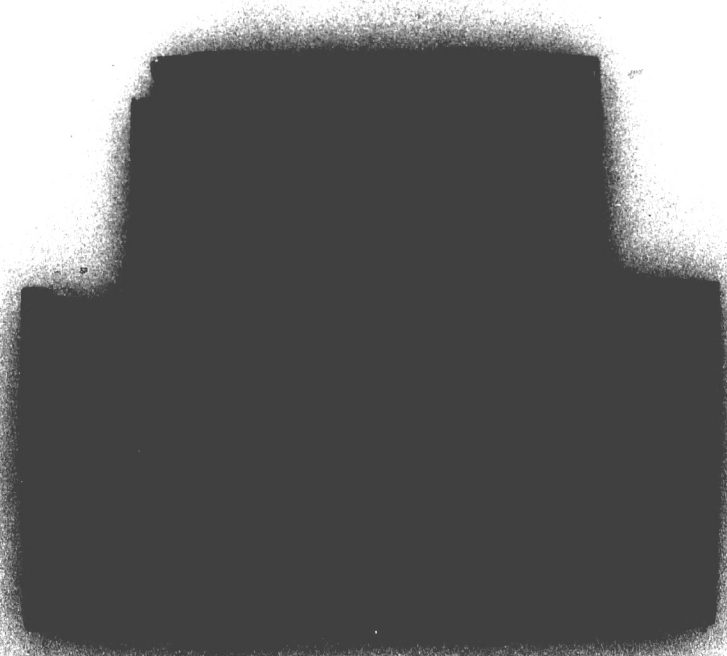

$\tau = 0.9$

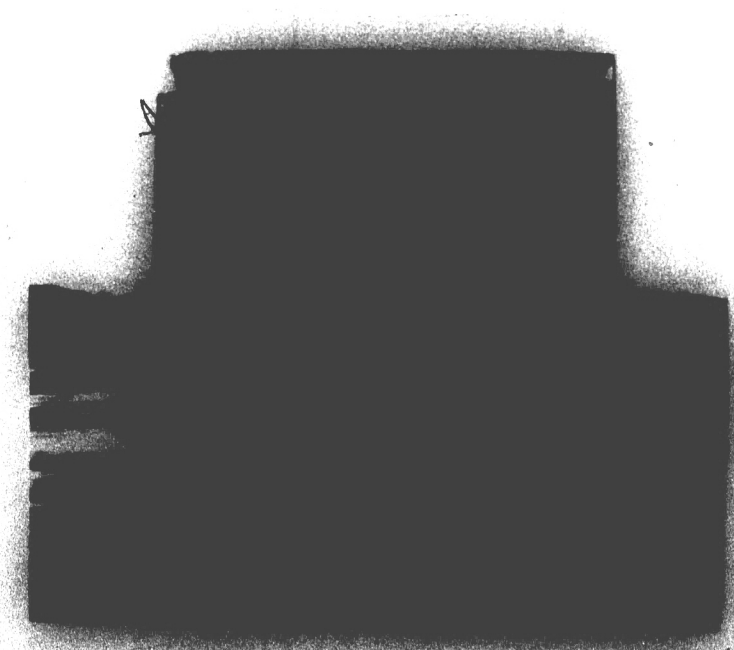

$\tau = 1.0$

Figure 10b

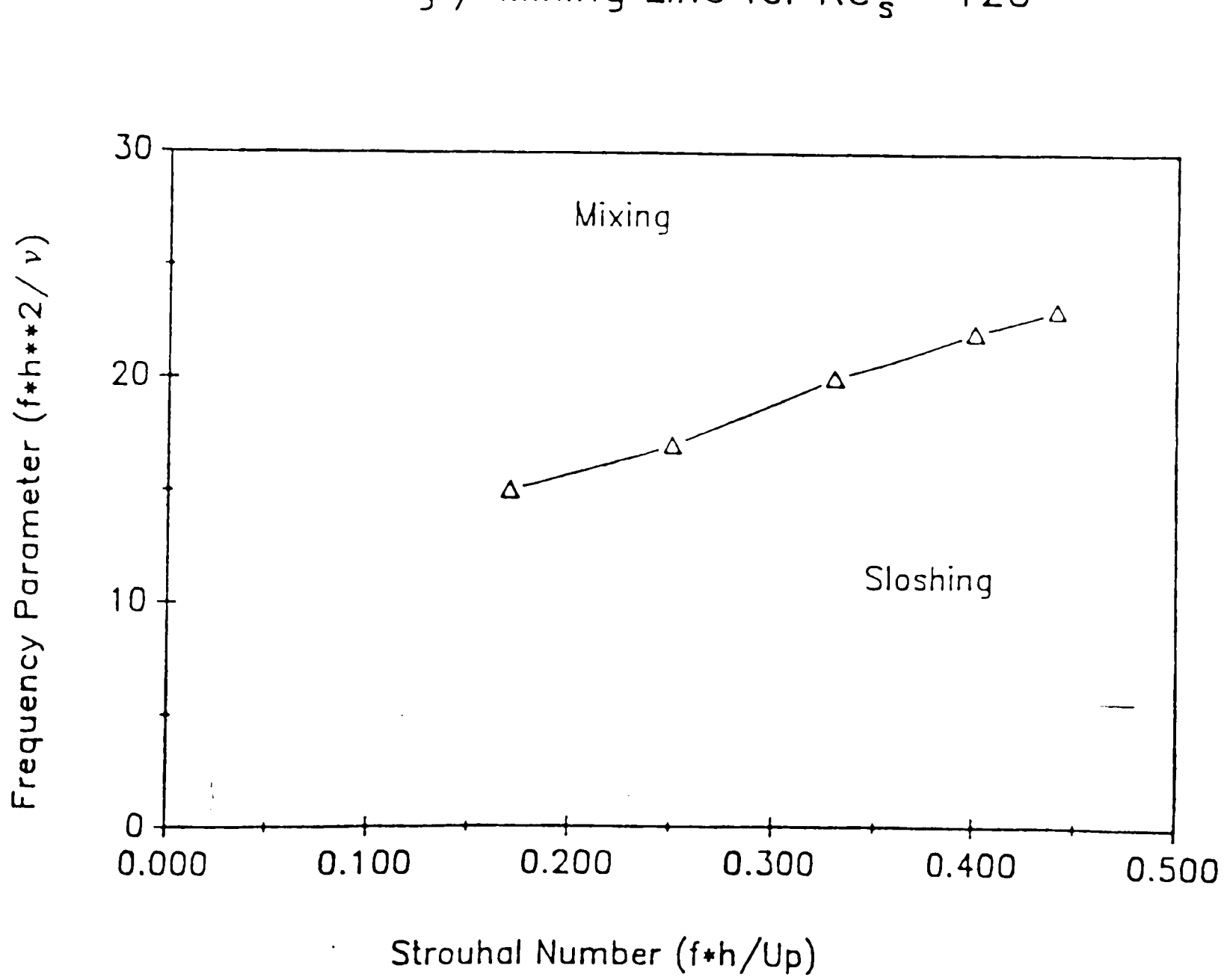
Sloshing / Mixing Line for Re_s = 120
30
20
10
0
Mixing
Sloshing
Frequency Parameter (f*h**2/ ν)
0.000
0.100
0.200
0.300
0.400
0.500
Strouhal Number (f*h/Up)

Figure 11

Sloshing / Mixing Lines
for Re_s = 50, 90, 120

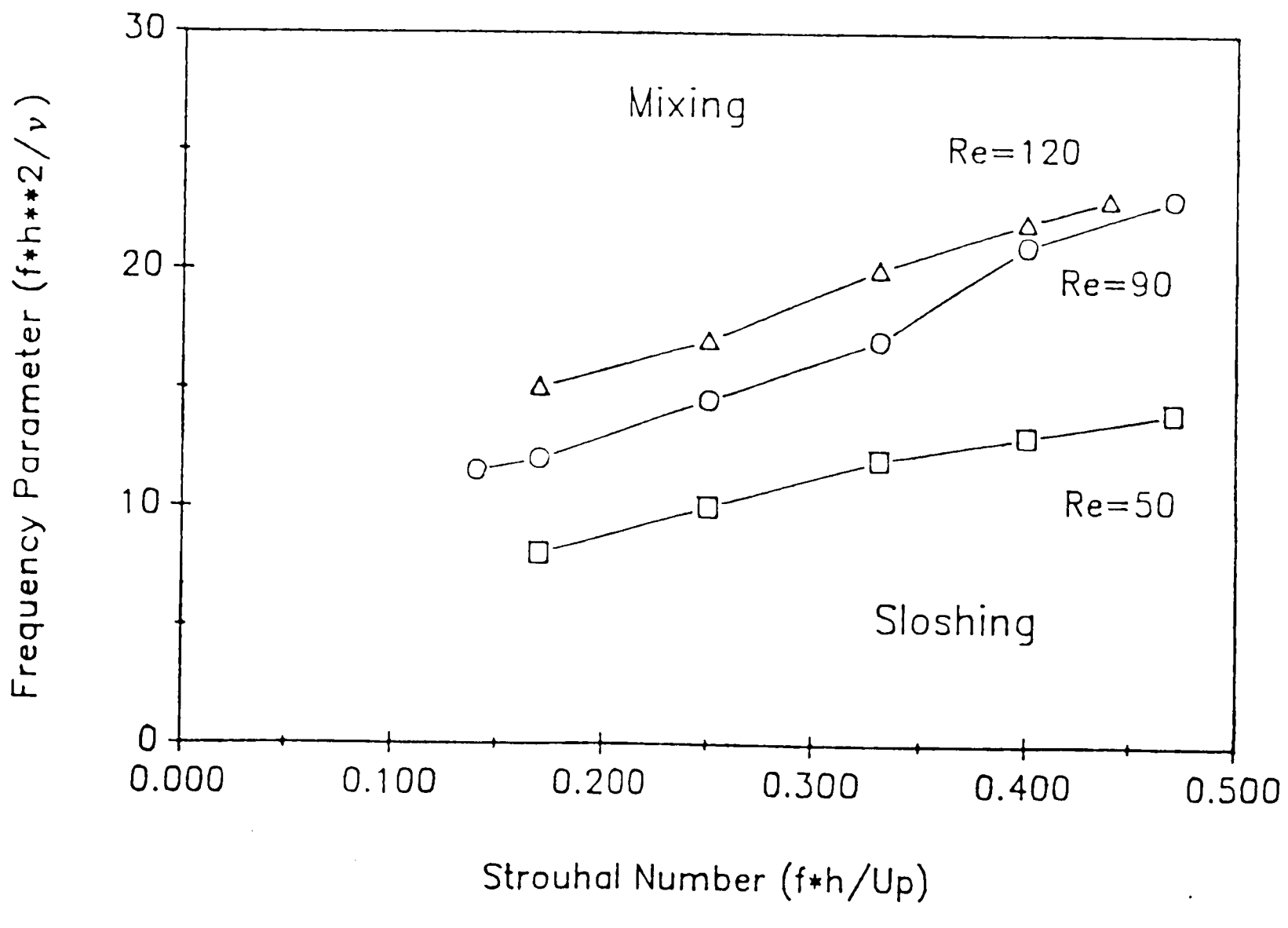

Figure 12

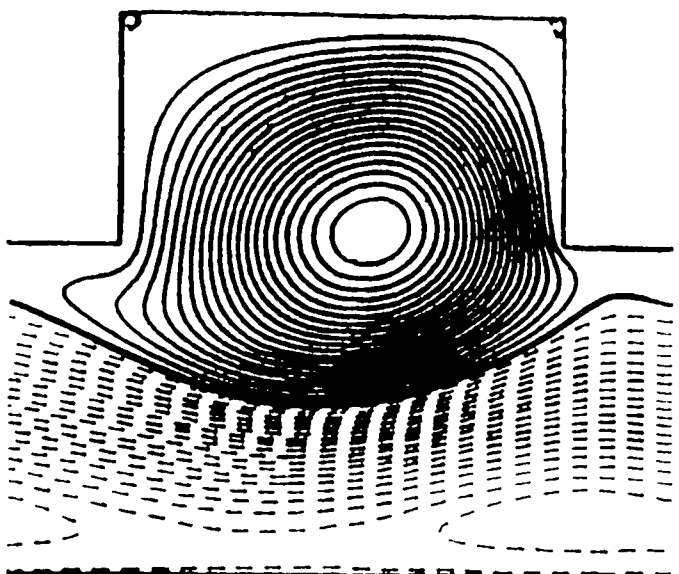
TIME= 6.00 MAX= .31
MIN= -.26

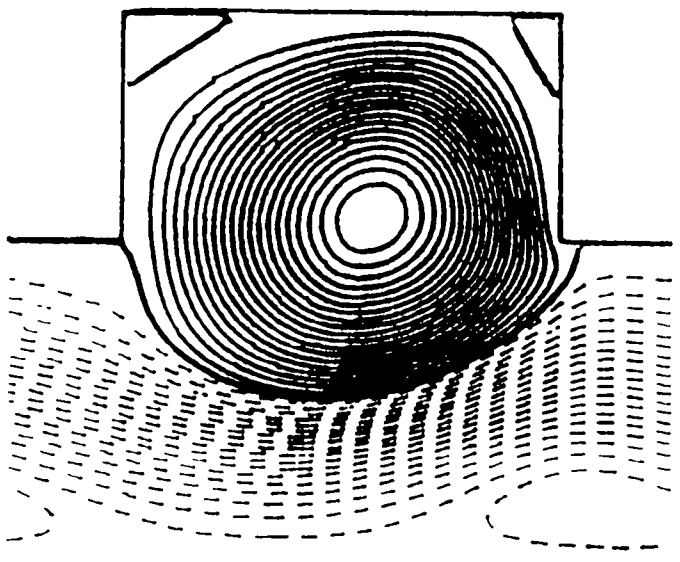
TIME= 6.10 MAX= .27
MIN= -.25

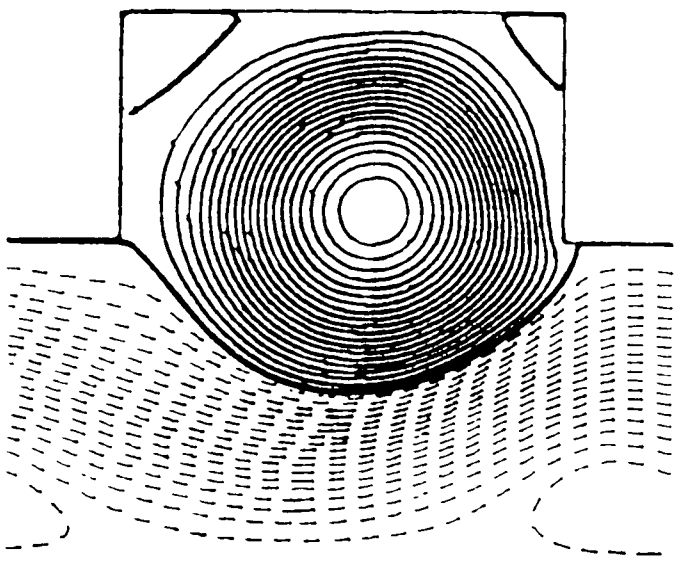
TIME= 6.20 MAX= .24
MIN= -.25

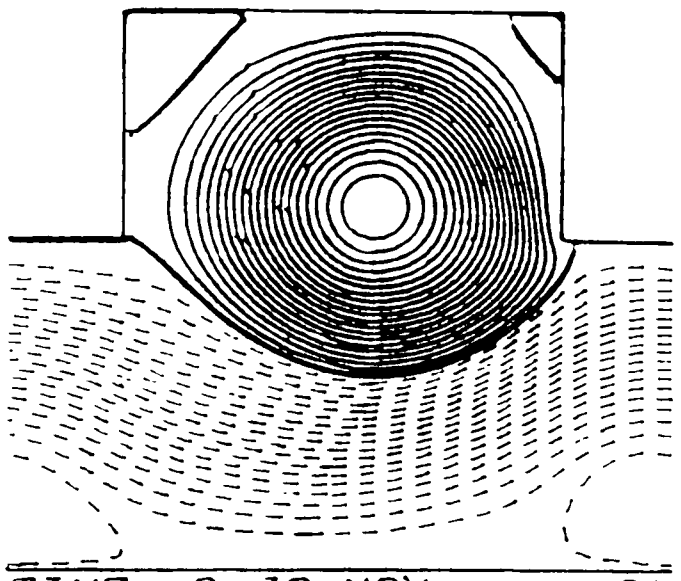
TIME= 6.30 MAX= .21
MIN= -.25

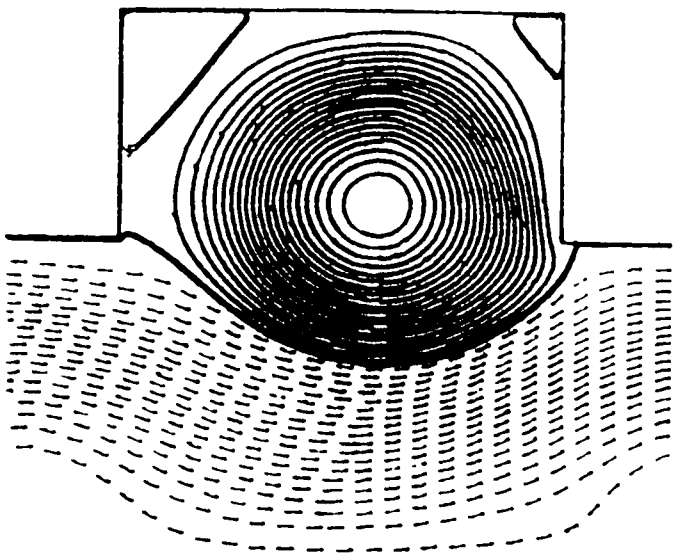
TIME= 6.40 MAX= .18
MIN= -.24

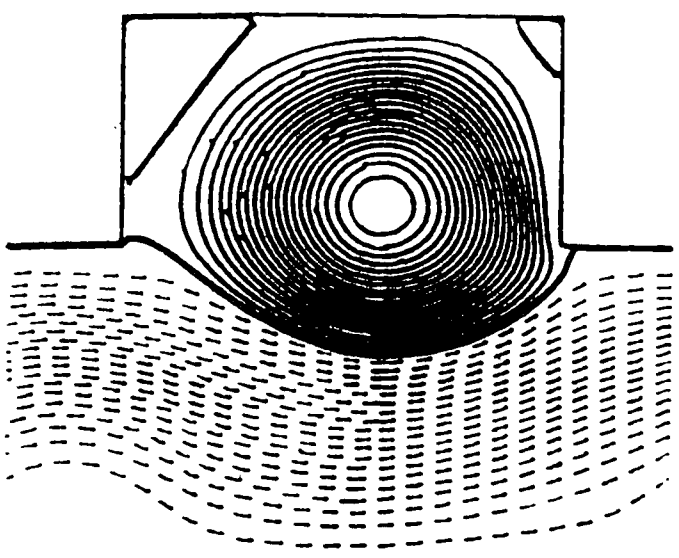
TIME= 6.50 MAX= .16
MIN= -.24

Figure 13a

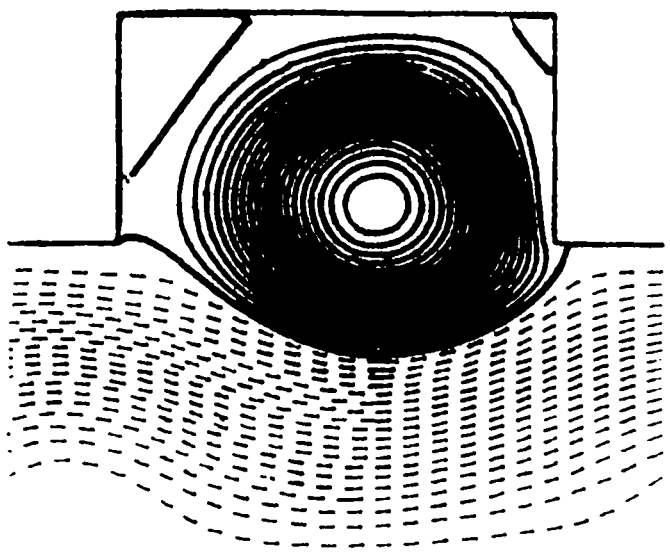

TIME- 6.50 MAX- .16
MIN- -.24

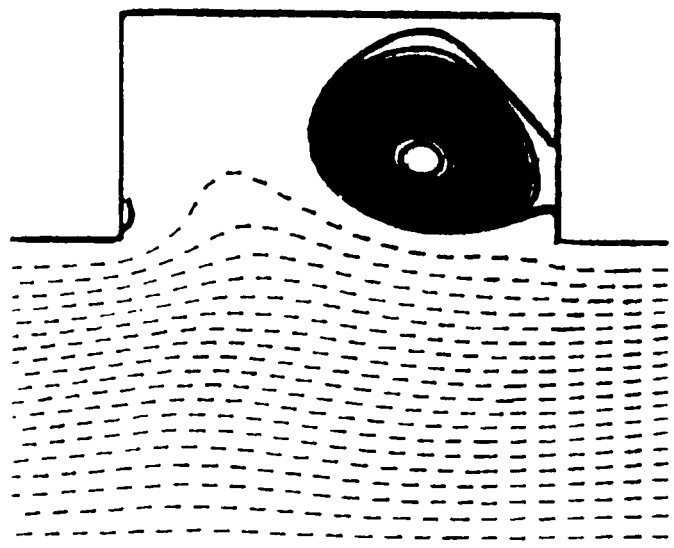

TIME- 6.60 MAX- .04
MIN- -.82

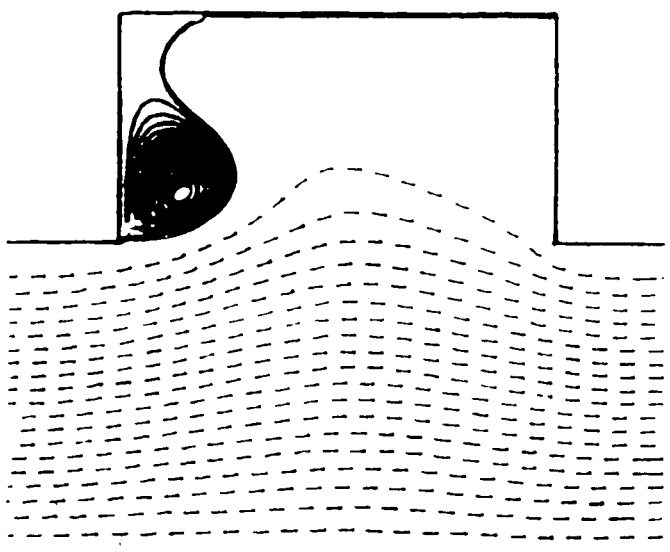

TIME- 6.70 MAX- .03
MIN- -1.18

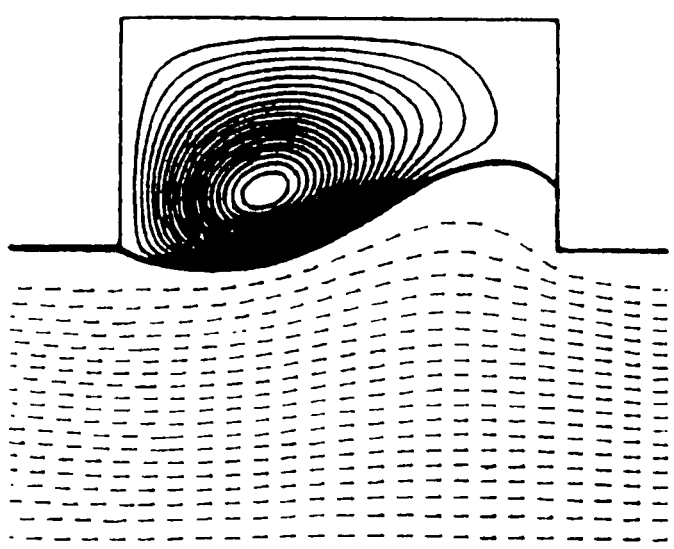

TIME- 6.80 MAX- .10
MIN- -1.18

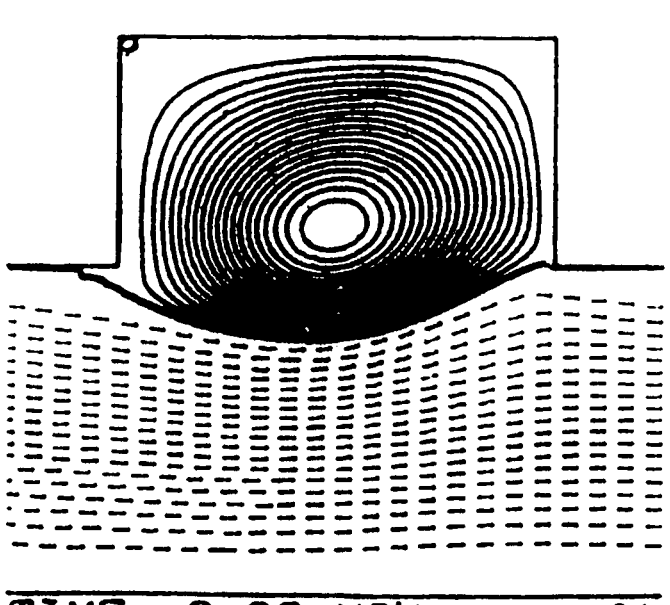

TIME- 6.90 MAX- .21
MIN- -.82

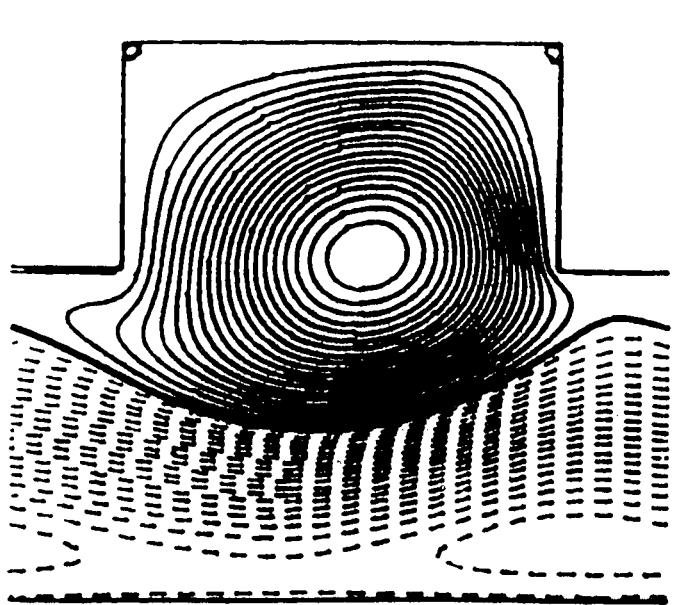

TIME- 7.00 MAX- .31
MIN- -.26

Figure 13b

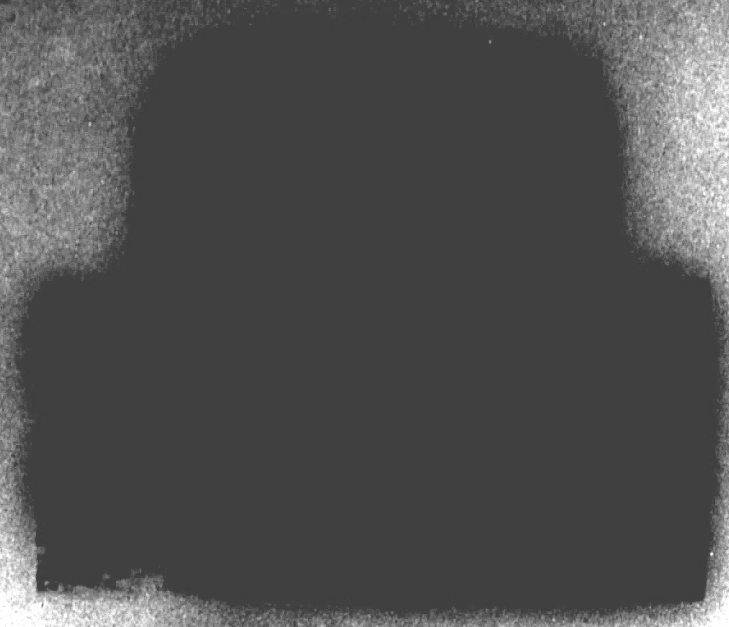

$\tau = 0.0$

$\tau = 0.1$

$\tau = 0.2$

$\tau = 0.3$

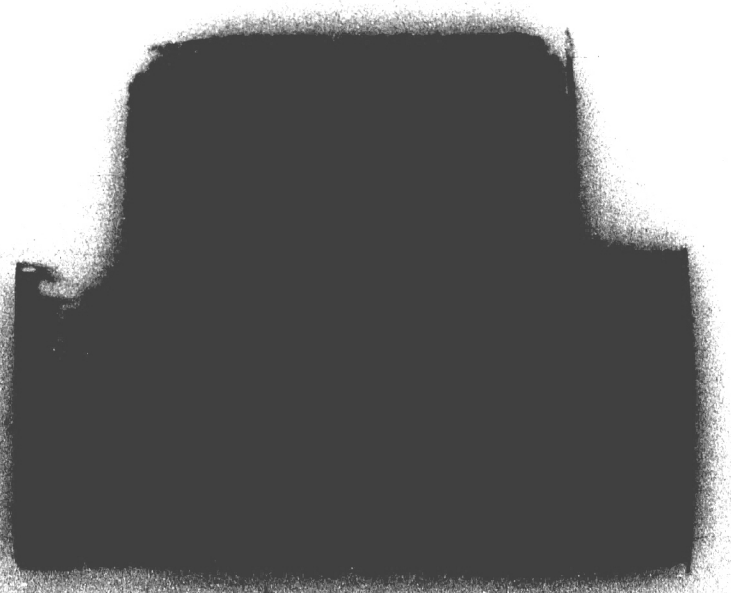

$\tau = 0.4$

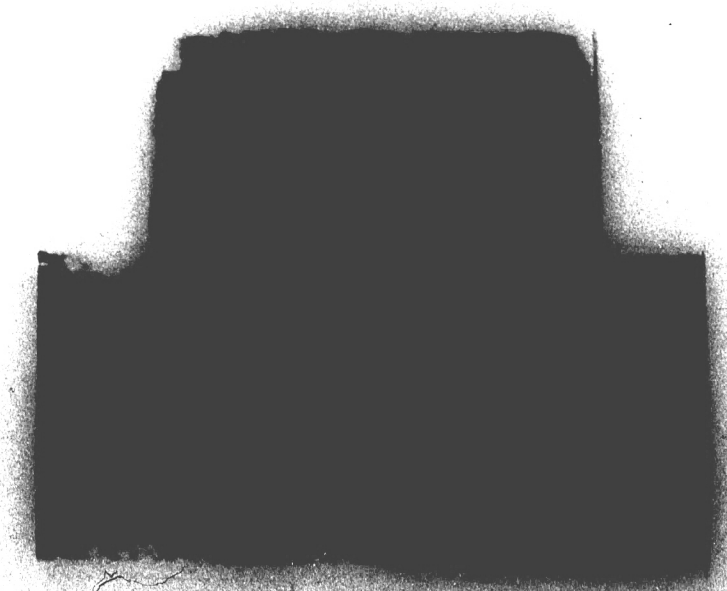

$\tau = 0.5$

Figure 14a

$\tau = 0.5$

$\tau = 0.6$

$\tau = 0.7$

$\tau = 0.8$

$\tau = 0.9$

$\tau = 1.0$

Figure 14b

References-

1- Sobey, I.J. 1980 On Flow Through Furrowed Channels. Part 1. Calculated Flow Patterns. Journal of Fluid Mechanics. **96**, 1.

2- Stephanoff, K.D., Sobey, I.J., and Bellhouse, B.J. 1980 On Flow Through Furrowed Channels. Part 2. Observed Flow Patterns. Journal of Fluid Mechanics. **96**, 27.

3- Sobey, I.J. 1982 Oscillatory Flows at Intermediate Strouhal Number in Asymmetric Channels. Journal of Fluid Mechanics. **125**, 359.

4- Kraus, A.D. and Bar-Cohen, A. 1983 Thermal Analysis and Control of Electronic Equipment. Hemisphere Publishing Corporation.

5- Ralph, M.E. 1986 Oscillatory Flows in Wavy-walled Tubes. Journal of Fluid Mechanics. **168**, 515.

6- Ghaddar, N.K., Korczak, K.Z., Mikic, B.B., and Patera, A.T. 1986 Numerical Investigation of Incompressible Flow in Grooved Channels. Part 1. Stability and Self-sustained Oscillations. Journal of Fluid Mechanics. **163**, 99.

7- Greiner, M. 1986 Experimental Investigation of Resonance and Heat Transfer Enhancement in Grooved Channels. Ph.D. Dissertation, Massachusetts Institute of Technology.

8- Roache, P.J. 1982 Computational Fluid Dynamics. Hermosa Publishers.

9- Savvides, C.N. and Gerrard, J.H. 1984 Numerical Analysis of the Flow Through a

Corrugated Tube With Application to Arterial Prostheses. Journal of Fluid Mechanics. **138**, 129.

10- Fromm, J. 1964 The Time Dependent Flow of an Incompressible Viscous Fluid. Methods in Computational Physics. **3**, 345.

11- Cheng, L.C., Robertson, J.M., and Clark, M.E. 1974 Calculation of Plane Pulsatile Flow Past Wall Obstacles. Computers & Fluids. **2**, 363.

12- Peyret, R. and Taylor, T.D. 1986 Computational Methods for Fluid Flow. Springer-Verlag.

13- de Vahl Davis, G. and Mallinson, G.D. 1976 An Evaluation of Upwind and Central Difference Approximations by a Study of Recirculating Flow. Computers and Fluids. **4**, 29.

14- Bozeman, J.D. 1973 Numerical Study of Viscous Flow in a Cavity. Journal of Computational Physics. **12**, 348.

15- Gupta, M.M. and Manohar, R.P. 1979 Boundary Approximations and Accuracy in Viscous Flow Computations. Journal of Computational Physics. **31**, 265.

16- Ghaddar, N.K., Magen, M., Mikic, B.B., and Patera, A.T. 1986 Numerical Investigations of Incompressible Flow in Grooved Channels. Part 2. Resonance and Oscillatory Heat-Transfer Enhancement. Journal of Fluid Mechanics. **168**, 541.

Vita-

J.S. Perkins was born May 15, 1964, in Springfield, Pennsylvania to parents John S. and Sandra R. Perkins. After graduating from Springfield High School in June, 1982, he began undergraduate work towards a B.S. in Mechanical Engineering at Lehigh University in Bethlehem, Pennsylvania. In June of 1986, he received his B.S.M.E. and worked briefly for the Harrison Radiator Division of General Motors. He then returned to Lehigh where he received a M.S. in Mechanical Engineering in January, 1989.